Nanoscale Res Lett (2007) 2:519–545
DOI 10.1007/s11671-007-9091-3

NANO REVIEW

Strategies for Controlled Placement of Nanoscale Building Blocks

Seong Jin Koh

Received: 2 June 2007 / Accepted: 20 August 2007 / Published online: 9 October 2007

Abstract The capability of placing individual nanoscale building blocks on exact substrate locations in a controlled manner is one of the key requirements to realize future electronic, optical, and magnetic devices and sensors that are composed of such blocks. This article reviews some important advances in the strategies for controlled placement of nanoscale building blocks. In particular, we will overview template assisted placement that utilizes physical, molecular, or electrostatic templates, DNA-programmed assembly, placement using dielectrophoresis, approaches for non-close-packed assembly of spherical particles, and recent development of focused placement schemes including electrostatic funneling, focused placement via molecular gradient patterns, electrodynamic focusing of charged aerosols, and others.

Keywords Placement · Array · Alignment · Nanoscale building blocks · Nanoparticle · Nanocrystal · Quantum dot · Nanowire · DNA · Protein · Carbon nanotube · Template · Electrostatic · SAMs · Dielectrophoresis · Capillary force · Growth

Introduction

There has been a lot of interest recently in fabricating electronic, optical, and magnetic devices/sensors that are built on nanoscale building blocks such as nanoparticles, nanowires, carbon nanotubes, DNA, proteins, etc. Over the past decade, very promising performances have been demonstrated at the single device level or in a collection of a few single units [1–14]. Despite these successes, a major challenge remains: for the individual functional units to be incorporated into practical devices and sensors, they must be placed onto exact substrate locations so that they can be addressed and connected among themselves and to the outside world. This, i.e., the precise placement of nanoscale building blocks on exact substrate locations, is an extremely challenging goal. This article reviews recent progress in a variety of placement strategies, some of which are nearing maturity, while others are in their infant stages [15]. Specifically, this review will discuss the following: (1) *Placement using physical templates*, employing capillary forces, spin-coating, surface steps, and others. This section also discusses template-assisted growth of quantum dot arrays; (2) *Placement using molecular templates*, employing patterned self-assembled monolayers (SAMs), whose specific terminal groups are functionalized to selectively interact with the building blocks; (3) *Placement using electrostatic templates*, employing localized charges on the substrate surface to attract charged building blocks; (4) *DNA-programmed placement*, employing 2D DNA crystals as scaffolds; (5) *Placement using dielectrophoresis*; (6) *Non-close-packed assembly of spherical particles*; and (7) *Focused placement*, employing focusing mechanisms to guide nanoscale building blocks to substrate locations which are smaller than the template guiding them.

The strategies that we will discuss in this article are not limited to *absolute* placement in the fixed substrate coordinates, but include *relative* positioning of nanoscale entities with respect to each other or to some reference structures. An example is a formation of 2D nanoparticle or protein arrays using a scaffold of 2D DNA crystal; *relative* positions between nanoparticles or proteins *within* the 2D

S. J. Koh (✉)
Department of Materials Science and Engineering,
The University of Texas at Arlington, Arlington, TX 76019,
USA
e-mail: skoh@uta.edu

DNA scaffold are well defined, although placement of DNA scaffolds themselves on the substrate is not easily controlled. We will also cover the *growth* or *formation* (rather than *placement*) of nanoscale entities that organize into an ordered form in one- or two-dimension. Formation of 2D quantum dot arrays using physical templates and growth of nanowires along the step edges belong to this category.

Placement Using Physical Templates

Physical templates can be utilized for controlled placement of nanoscale or microscale building blocks. Examples of physical templates include holes and trenches that can be fabricated on a substrate surface using lithography and etching/lift-off techniques, surface steps that naturally exist on crystalline metal and semiconductor surfaces, corrugation of substrate surfaces, and channels formed in a microstamp for molecular printings. In this section, we will review several strategies to position nanoscale and microscale building blocks using these physical templates.

Capillary Force Driven Placement into Physical Templates

Capillary force has been successfully exploited to place individual nanoscale/microscale building blocks into trenches or holes pre-defined on the substrate. In this approach [16–20], the substrate is immersed into a colloidal solution, and then slowly pulled out or slowly dried by solvent evaporation through heating. In both cases, the solution–air interface slowly recedes. At the front of the receding interface, the thickness of solution becomes smaller than the diameter of nanoparticles (for non-spherical shape, the height of the building blocks) and a three-phase solution–air–nanoparticle interface is formed around the nanoparticle surfaces. This three-phase interface creates capillary forces on the nanoparticles. The direction of the capillary force depends on thickness of the solution layer, which depends on the substrate pattern, thicker in the trenches or holes. The net result is that the nanoparticles are pushed into the trenches or holes while they pass through other areas without any deposition.

This capillary force driven placement has been successfully demonstrated by many groups. Xia et al. demonstrated uniform 1D and 2D aggregates of colloidal particles characterized by a range of well-defined sizes, shapes, and structures [16, 20]. Figure 1 shows one example of their accomplishments where polystyrene (PS) beads and gold nanoparticles were placed along the trench lines. In addition, by systematically changing the geometric shape of the template and the size of the colloidal spheres, they were able to place colloidal particles into templates and form aggregates in well-controlled configurations [16]. With appropriate template design, such as using V-shaped grooves, they placed spherical colloids into multi-layered aggregates such as helical chains [19]. Alivisatos and co-workers showed that the capillary forces are still effective for the placement of nanoparticles below 50 nm [17]. They showed organization of nanoparticles of 50-, 8-, and 2-nm in diameter into lithographically defined trenches and holes. Placement of non-spherical shape building blocks such as CdTe nanotetrapods has also been demonstrated.

Particle aggregates composed of different types of particles (different in size, chemical composition, surface functionality, density or sign of surface charges, etc.) have also been assembled using capillary force driven placement. Xia and co-workers demonstrated the formation of asymmetric dimers composed of two different kinds of particles [21]. In their approach, they first prepared an array of cylindrical holes (diameter: 5.0 μm, height: 2.5 μm) in

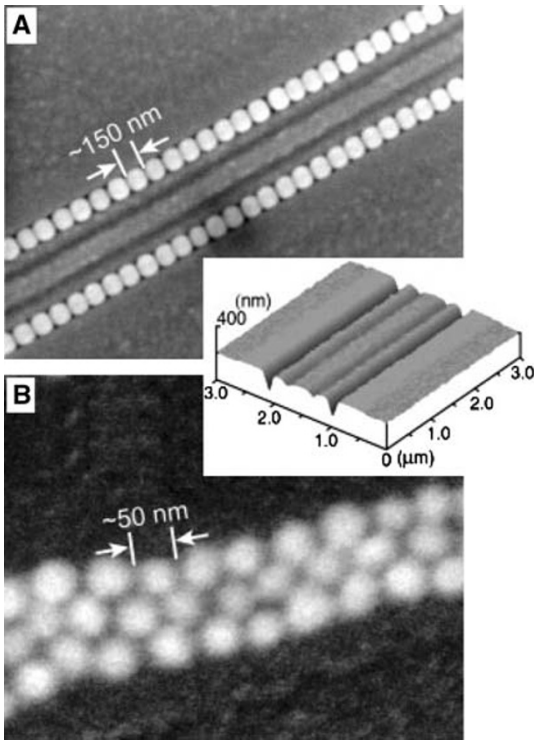

Fig. 1 SEM images of (**A**) two linear chains of 150 nm PS beads and (**B**) a stripe of closely packed lattice of gold nanoparticles (~50 nm in diameter) that were formed by templating against trenches 120 nm × 150 nm in cross-section (see the inset for an AFM image). The trenches were, in turn, fabricated using near-field optical lithography with an elastomeric stamp as the binary phase shift mask. (Reprinted with permission from Reference [16]. Copyright 2003 Wiley-VCH.)

photoresist film spin-coated on a glass substrate, and then single 2.8-μm PS beads were trapped inside each hole, Fig. 2A. This was achieved by a careful choice of the diameter and height of the holes as well as the particle diameter. Under this geometrical constraint, during the drying process, capillary force pushed a single PS particle into each hole one by one. After fixing the position of the PS beads inside the holes by heating the sample to a temperature slightly higher than the glass transition temperature of PS (~93 °C), the sample went through a 2nd dewetting process where 1.6-μm single silica colloids were positioned into the remaining space of each hole due to the capillary force, Fig. 2B. These asymmetric dimers can be permanently welded onto single pieces by heating the sample at temperature slightly higher than the glass transition temperature of PS. The seamless bonding of the dimers can be seen in the TEM image, Fig. 2C, which was obtained after the removing the photoresist film. This approach allows controlled fabrication and placement of many other combinations of asymmetric dimers. An example is displayed in Fig. 2D.

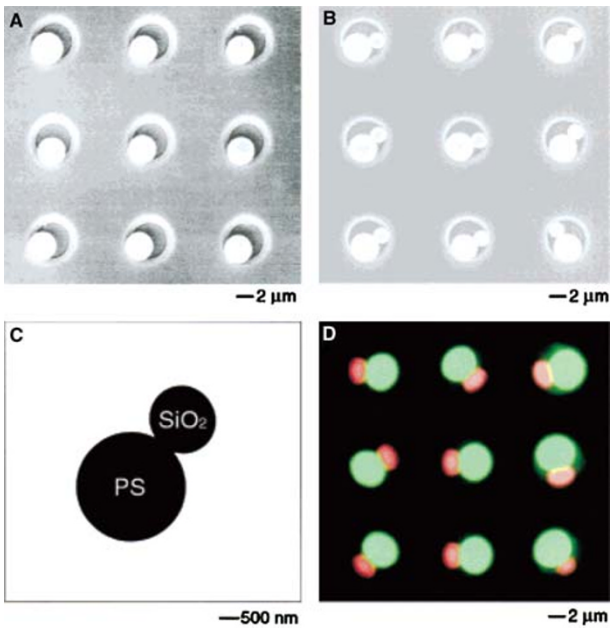

Fig. 2 (**A**, **B**) SEM images that illustrate the procedure used to assemble two different types of spherical colloids (2.8-μm PS beads, 1.6-μm silica balls) into dimeric units. The cylindrical holes were patterned in a thin film of photoresist. (**C**) TEM image of one of the dimers after released from their original support by dissolving the photoresist pattern in ethanol, followed by redeposition onto a TEM grid. (**D**) The fluorescence microscopy image of a 2D array of dimers that were self-assembled from PS beads that were different in both size and color: 3.0-μm beads doped with a green dye (FITC) and 1.7-μm beads doped with a red dye (Rhodamin). (Reprinted with permission from Reference [21]. Copyright 2001 American Chemical Society.)

Formation of Quantum Dot (QD) Arrays Using Physical Templates

Quantum dots (QDs) are nanoscale objects in which electrons are confined in a dimension that is smaller than their de Broglie wavelength, resulting in the change of energy gaps or creation of quantized energy levels much like individual atoms (therefore, QDs are sometimes called artificial atoms) [22–24]. QDs have been of great interest due to their promising applications such as quantum electronic/optical devices [25–27], single electron devices [3], and single photon sources [28–30]. Among many methods, the formation of QDs in the heteroepitaxial growth of thin films using molecular beam epitaxy (MBE) has been most extensively studied. The usual growth mode is Stranski-Krastanow (SK) growth, in which self-assembled QDs are formed via 2D to 3D transition of epitaxial films in heteroepitaxial growth of lattice mismatched materials. This transition occurs spontaneously to reduce the misfit strain in the 2D strained heteroepitaxial wetting layers by forming dislocation-free 3D islands (QDs). Various QD systems have been grown using SK growth mode including Ge QDs on Si (001), GaAs QDs on GaAs (001), and InAs/InGaAs QDs on GaAs (001) [31–33].

The QDs produced as above, however, are randomly distributed over the surface and control of positioning has been difficult. For practical applications where individual QDs must be addressable, including integrated systems on single chips and single QD devices, it is required to grow QDs at exact locations. Among many strategies to grow QDs with precise position control, the template-assisted SK growth (specifically, the SK growth of QDs on pre-patterned substrates) has been shown to be very promising as demonstrated by many recent studies [30, 34–44]. This section briefly reviews recent advances in this strategy.

One method to grow well-ordered QD arrays is to use selective epitaxial growth (SEG) on a patterned substrate. In this approach, the substrate surface is masked with a material different from the substrate, and upon exposure to source gases, QDs grow only on the unmasked exposed surface, leading to a QD array in the original mask pattern. For example, well-ordered Ge QD arrays were grown on Si (001) by Kim et al. [44]. They first made a square array of windows in SiO_2 film (thickness 50 nm) on a Si (001) substrate. After selective deposition of a Si buffer layer on the exposed Si substrate, selective SK growth of Ge on the Si buffer layer was carried out. With a window size of 300 nm or below, they were able to grow exactly one Ge QD at the center of each window with excellent size uniformity, which was attributed to nucleation and diffusion kinetics, and/or strain energetics. Importantly, using this method, the size of the QDs can be made smaller than that of exposed windows.

Well-positioned QD arrays can also be made without resorting to any masks, but relying on surface templates. For example, Bauer and co-workers first made 2D periodic pits on a Si (100) surface using lithography and RIE, which was followed by deposition of a Si buffer layer [38]. Subsequent deposition of 4–10 monolayers (MLs) of Ge led to the formation of precisely positioned QD arrays having the same ordering as the underlying template. Figure 3 demonstrates AFM topographies and their Fourier transforms (FT) of well-positioned QD arrays for 10 ML Ge and 6 ML Ge deposition. The preferential growth of Ge QDs at the center of the pits was attributed to the fast downward diffusion of Ge dimers and accumulation of Ge atoms at the bottom of the pits. Because the area at the pit bottom was small, only one QD was formed per each pit.

Formation of well-positioned QD arrays can also be realized on almost flat surfaces that are made by deposition of buffer layers/spacers on pre-patterned substrates [37, 40, 45–47]. The key to controlled positioning of the QDs is to use the long-range order of the underlying pre-patterns to produce appropriate strain fields in the subsequent layers. The pre-patterns are defined using typical lithography and etching/lift-off. Then, buffer layers/spacers are deposited over them, resulting in a film which is nearly flat and which bears modulated strain fields that have the same lateral 2D ordering as the underlying pre-patterns. The strain field causes strain-modulated diffusion of deposited adatoms as well as accumulation/preferential nucleation of adatoms in the area of minimum strain energy density [41, 46, 48, 49]. This leads to the formation of QDs in a long-range ordered array which is a replica of the underlying pre-patterns. Kiravittaya et al., for example, demonstrated formation of near-perfect QD arrays [34, 37, 46]. A representative AFM image is shown in Fig. 4, where a square array of InAs QDs was grown on a patterned GaAs (001) substrate [34, 37]. This highly ordered positioning of QDs was also achieved for other systems such as Ge QDs on Si (001) and InGaAs QDs on GaAs (001) [40, 47]. With this method, QDs can be positioned over a large area in parallel processing. For example, Heidemeyer et al. demonstrated a growth of a QD array composed of about one million InGaAs QDs with near-perfect (99.8% yield) site control [47]. In addition, QD formation on pre-patterned substrates produced superior shape and size uniformity compared to growth on unpatterned substrates. A very narrow size distribution, ~5% in height and diameter, was demonstrated for InAs QDs on GaAs (001), Fig. 4C [34, 37].

The formation of precisely positioned QD arrays is not limited to 2D arrays, but can be realized for 1D and 3D arrays as well. One-dimensional QD arrays were formed utilizing modulated strain fields created by underlying pre-patterned trenches [39, 45, 50, 51]. The capability of

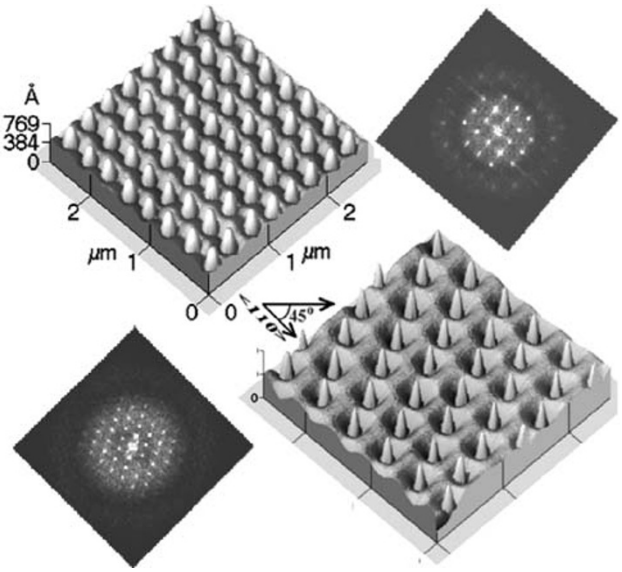

Fig. 3 3D AFM topographies of the islands and their Fourier transforms. Top: 3D AFM image of a sample with 10 ML Ge deposition (top left) and its Fourier transform (top right). Period: 370 nm × 370 nm, along ⟨110⟩ directions. Bottom: 3D AFM image of a sample with 6 ML Ge deposition (bottom right) and its Fourier transform (bottom left). Period: 400 nm × 400 nm, along [110] and [100] directions. (Reprinted with permission from Reference [38]. Copyright 2004 American Institute of Physics.)

forming ordered 2D QD arrays can be utilized to form 3D QD crystals through stacking of 2D QD arrays. Formation of 3D QD crystals was demonstrated for InAs/GaAs QDs on patterned GaAs (001) [36, 46] and for Ge QDs on patterned Si (001) [40]. The capability of growing QDs on exact substrate locations has significant implications for the realization of practical quantum devices. For example, Kiravittaya et al. grew ordered GaAs QD arrays on GaAs (001) and demonstrated single photon emission from the ordered QDs [30]. The formation of addressable QDs could lead to fabrication of integrated single QD devices.

Other Placement Schemes Utilizing Physical Templates

In addition to the capillary force assisted method and formation of QD arrays using pre-patterns, spin-coating assisted placement, assembly along the step edges of the surface, and sonication-assisted solution embossing are examples of other placement schemes using physical templates. Brueck and co-workers explored spin-coating to place sub-100 nm silica particles into holes and grooves patterned on silicon oxide film or a silicon wafer [52]. They showed that the controlled placement of spherical particles can be achieved by choosing appropriate spin speed, the pH, and the geometries of grooves and holes (width, depth,

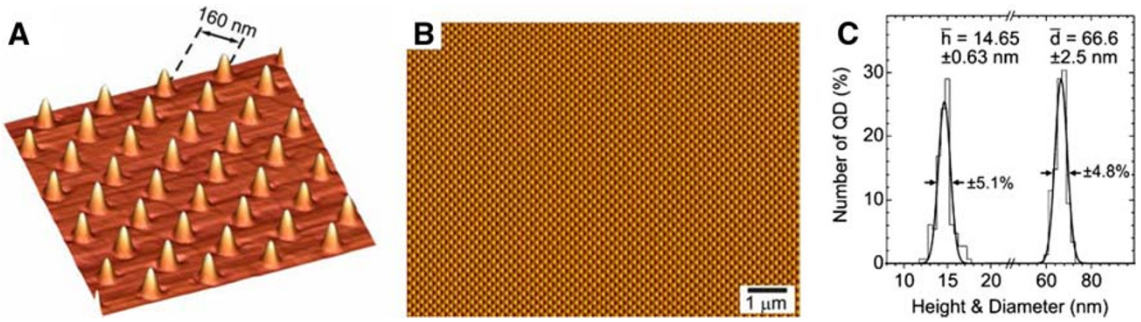

Fig. 4 (**A**) 3D view AFM image of a homogeneously ordered InAs QD array on flat GaAs surface. (**B**) Large area AFM image of the same sample. (**C**) Height and diameter distributions extracted from the AFM image. (Reprinted with permission from Reference [34]. Copyright 2006 Springer.)

diameter, and the sidewall slope). By adjusting these parameters, they formed one-particle wide linear chains, zigzag chains (1.5 particle wide), and two-column arrays of ~80 nm silica nanoparticles inside pre-defined grooves.

Step edges, which naturally exist on the surface of crystalline metals or semiconductors, can be utilized as templates along which nanowires of various materials can be grown. In this approach, the atoms are deposited onto the substrate surface in ultrahigh vacuum (UHV) and diffuse to atomic step edges, forming nanoscale wires. The width of nanowires and the spacing between them can be independently controlled by varying deposition time and step spacing (via miscut angle), respectively. By controlling the surface diffusion of Cu atoms on Pd(110) surface, Röder et al. demonstrated the formation of monatomic one-dimensional Cu chains along the step edges of a Pd(110) surface [53], Fig. 5. Gambardella et al. demonstrated high-density parallel arrays of regularly spaced nanowires by systematically controlling the growth kinetics [54]. They showed regularly spaced monatomic rows of Ag and Cu along step edges of a Pt(997) surface. Nanowire formation has been demonstrated for other systems including Cu nanowires on step edges of a Mo(110) surface [55–57] and Cu nanowires on step edges of a W(110) surface [55, 58].

Electrodeposition of atoms along the surface step edge is another useful method for positioning of nanowires on the substrate. For example, Penner and co-workers utilized step edges on a graphite surface to produce metallic molybdenum nanowires [59]. Their approach involved two steps; first electrodeposition of molybdenum oxide (MoO_x) along step edges and reduction of MoO_x to metallic Mo wires by hydrogen treatment. Mo wires with diameters ranging from 15 nm to 1.0 μm and lengths up to 0.5 mm were produced along the step edges. A similar approach allowed nanowire formation along the step edges with other materials such as Fe_2O_3, Cu_2O, and Pd [60, 61]. The parallel alignment of Pd nanowires formed along the step edges was utilized by Penner and co-workers to fabricate hydrogen sensors [60].

Sonication-assisted solution embossing, recently reported by Stupp and co-workers, is a useful way for a simultaneous self-assembly, orientation, and patterning of one-dimensional nanostructures as demonstrated for the nanofibers of peptide-amphiphile molecules [62]. In their approach, a stamp made of polydimethylsiloxane (PDMS) was pressed and held onto a glass or silicon substrate in a beaker containing peptide-amphiphile nanofibers in water, trapping the nanofibers between the channels of the stamp and the substrate. The combined effect of solvent evaporation, ultrasonic agitation, and confinement within the channels of the PDMS stamp resulted in alignment of peptide-amphiphile nanofibers parallel to stamp channels.

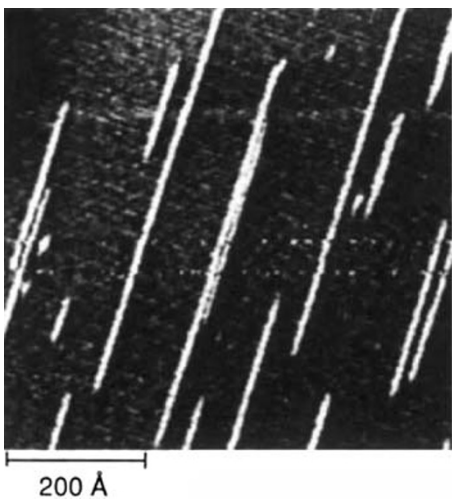

Fig. 5 STM (Scanning Tunneling Microscope) image of monatomic Cu wires grown on the Pd(110) surface; the one-dimensional copper chains were grown and imaged at 300 K, the total coverage was $\theta_{Cu} = 0.05$ ML. (Reprinted with permission from Reference [53]. Copyright 1993 Macmillan Publishers Ltd.)

Its capability of simultaneously orienting and patterning macromolecules may find many useful applications.

Placement Using Molecular Templates (SAMs)

Self-assembled monolayers (SAMs) are ordered assembly of organic molecules that spontaneously form on the surface of metals, metal oxides, and semiconductors [63–68]. The surface properties of SAMs can be engineered by selecting an appropriate tail group of the organic molecules comprising SAMs or modifying the tail group of existing SAMs with various techniques. Then, the substrate surface functionalized with localized patterns of SAMs can serve as templates onto which nanoscale or microscale building blocks are selectively attracted. There are many approaches for producing or modifying SAMs patterns and subsequent organization of the building blocks into the pattern areas. Since these are extensively reviewed by others [69–77], only some major approaches will be briefly described here.

The techniques for creating patterned SAMs can be categorized into three themes [69, 73]. First is to locally *attach* SAMs molecules onto desired substrate locations. This scheme includes microcontact printing (μCP) [78, 79], dip-pen nanolithography (DPN) [74, 80], and selective adsorption of specific SAMs molecules onto pre-defined substrate patterns [81, 82]. Second approach is to locally *remove* SAMs molecules from existing SAMs layer. This includes selective removal of SAMs using UV light [83, 84], STM-induced localized desorption of SAMs [73, 85, 86], and AFM-assisted localized removal of SAMs [73, 74, 77, 87–89]. For both themes, the exposed surface area having no SAMs can either be backfilled with other SAMs molecules or left bare. The third approach is to locally *modify* the terminal group of SAMs molecules, followed by selective functionalization and/or selective attachment of nanoscale building blocks [73, 88, 90–95].

An example of the first theme (patterning via attaching SAMs) is the μCP method [78, 79]. In this approach, organic molecules are inked onto an elastomeric stamp (typically made of polydimethylsiloxane (PDMS)) and transferred to the substrate surface by stamping. For example, alkanethiol molecules can be printed to form patterned SAMs on gold surfaces. Micrometer or submicrometer resolution patterns can be routinely obtained with this method. Selective placement of nanoscale or microscale building blocks onto the SAMs patterns were demonstrated for nanoscale or microscale particles, carbon nanotubes, nanowires, proteins, and DNA [96–100]. In another approach, target molecules (to-be-deposited molecules) themselves are inked onto the stamp and directly printed onto the SAMs-coated substrate surface utilizing specific binding between the target molecules and tail groups of SAMs molecules. For example, Whitesides and co-workers demonstrated patterned placement of biotin and benzenesulfonamide ligands onto SAMs of alkanethiolates on gold [101]. The merit of μCP is that it is a parallel process and allows placement of nanoscale objects over a large area in very short time. Another merit is that placement of building blocks is possible for flexible or even curved substrates [102].

Another example of the attaching scheme is dip-pen nanolithography (DPN), which was pioneered by Mirkin and co-workers [74, 80]. This method uses an atomic force microscope (AFM) tip to transport molecules adsorbed on the tip to precise substrate locations with resolution as high as a few tens of nanometers. The transported molecules spontaneously form self-assembled monolayers (SAMs) and SAMs patterns can be "written" as the AFM tip migrates across the substrate surface. This patterned area can be used as templates onto which nanoscale building blocks are selectively attached. The other way is to directly print the desired molecules (such as DNA and proteins) by inking the AFM tip with those molecules [103]. The SAMs pattern generated by DPN was used to place nanoparticles [104, 105], proteins [106], virus [107], and carbon nanotubes [96, 108, 109]. For example, Mirkin, Schatz, and their co-workers demonstrated placement of singe-walled carbon nanotubes (SWNTs) onto very thin lines (sub-100 nm) of SAMs patterns produced by DPN, Fig. 6 [109]. The SAMs patterns were made by writing 16-mercapto-hexadecanoic acid (MHA) on gold substrate using DPN, followed by passivating (backfilling) the rest of the surface with 1-octadecanethiol (ODT). When a drop of 1,2-dichlorobenzene containing SWNTs was applied on the substrate, the drop first wetted on the hydrophilic MHA pattern and then, during subsequent solvent evaporation, van der Waals interactions between SWNTs and the MHA-SAM drove the SWNTs to the boundary of MHA-SAM and ODT-SAM, resulting in well-controlled placement of SWNTs, Fig. 6. Placement of SWNTs in line shape, ring-shape, and more complex geometry was realized with sub-100-nm resolution.

An example of the second theme (patterning via removal of SAMs) is STM-assisted patterning [73, 85, 86]. There are several mechanisms for the STM-assisted removal of SAMs (or combinations of these) including mechanical removal by tip-surface interactions, electron-beam-induced degradation or desorption, field ionization, and field-enhanced surface diffusion. For example, Kim and Bard demonstrated patterning SAMs of *n*-Octadecanethiol (ODT) on a gold surface through mechanical removal by bringing the STM tip closer to the substrate and employing a low bias (10 mV) and high tunneling current (10 nA) [85]. Crooks and co-workers showed patterning of ODT SAMs with a resolution of 25 nm × 25 nm [86]. AFM can

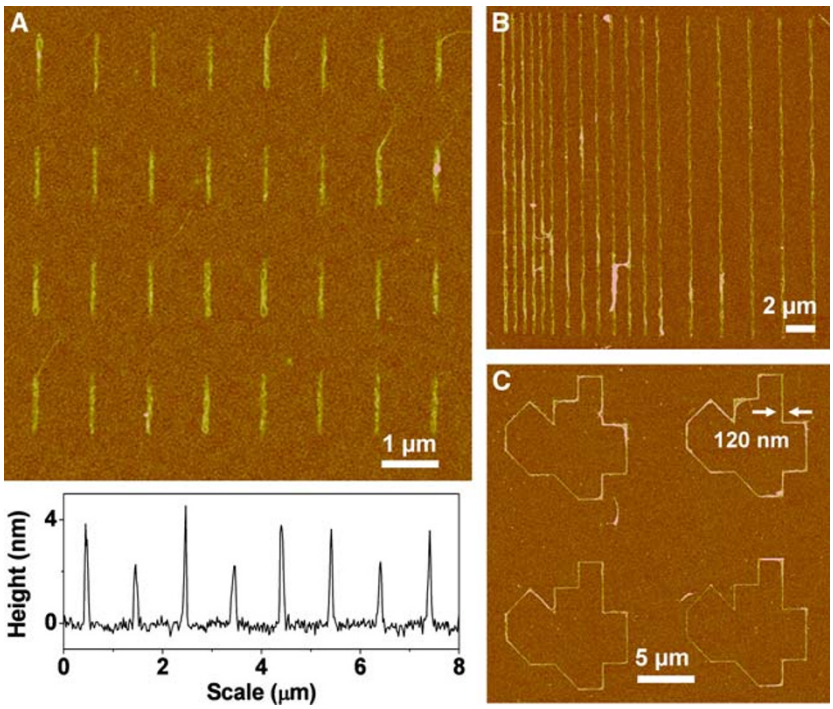

Fig. 6 AFM tapping mode topographic images of SWNT arrays. (**A**) Parallel aligned SWNTs with a line density approaching $5.0 \times 10^7/cm^2$. (**B**) Linked SWNTs following MHA lines (20 μm × 200 nm) spaced by 2 μm, 1 μm, and 600 nm. (**C**) Random line structure, showing the precise positioning, bending, and linking of SWNTs to a MHA affinity template. All images were taken at a scan rate of 0.5 Hz. The height scale is 20 nm. (Reprinted with permission from Reference [109]. Copyright 2006 National Academy of Sciences, U.S.A.)

also be utilized to locally remove SAMs [73, 74, 87–89]. The SAMs can be mechanically removed by the AFM tip, a process sometimes called nanoshaving. For example, Liu and co-workers demonstrated AFM-assisted removal of alkanethiol SAMs on a Au surface, followed by selective attachment of thiol-passivated Au nanoparticles onto exposed SAMs patterns [89]. Another type of AFM-assisted patterning involves removal of SAMs and simultaneous oxidation of the exposed substrate surface, named local oxidation nanolithography (LON) [77, 87]. LON is based on localized oxidation reaction that occurs within a water meniscus formed between an AFM tip and the substrate surface. Lateral resolution of several tens of nanometers can be obtained with LON [110]. The localized oxide pattern was utilized as templates to place nanoscale objects such as single-molecule magnets [87].

The third theme of SAMs patterning involves modifying the tail group (terminal group). The SAMs tail group can be locally modified using various techniques such as focused electron beam irradiation [111, 112], ultraviolet (UV) light irradiation [93, 94, 113, 114], and AFM [88, 90–92, 94, 95]. The modified tail group can be used directly as templates onto which the building blocks attach or further functionalized by attaching other molecules. For example, Calvert et al. used deep UV irradiation to modify and pattern organosilane SAMs [93]. The UV-modified pattern was further functionalized by reacting with other molecules. The patterned SAMs were utilized as templates to attract fluorophores, metals, and biological cells such as human SK-N-SH neuroblastoma cells. Sagiv and co-workers utilized a conductive AFM tip to locally modify the SAMs of *n*-octadecyltrichlorosilane (OTS) on silicon substrate and selectively attach Au nanoparticles onto the modified patterns [91]. In this approach, named constructive nanolithography [90], the voltage bias applied to the AFM tip induced local electrochemical reaction converting the terminal group of OTS ($–CH_3$) to carboxyl (–COOH). The tip-inscribed –COOH patterns were further functionalized with nonadecenyltrichlorosilane (NTS) via photoreaction and reduction, producing bilayer SAMs patterns terminated with amine group ($–NH_2$; $–NH_3^+$), Fig. 7A. When the substrate was immersed into a colloid containing negatively charged Au nanoparticles, they selectively attached onto the amine terminated patterns via the electrostatic interaction, Fig. 7A. They demonstrated placement of Au nanoparticles (diameter 17 nm or 2–6 nm) onto the amine terminated patterns, forming 2D square arrays, letters, and more complex nanoarchitecture, Fig. 7C.

As a final note for this section, it is appropriate to point out that the scanning probe techniques, like other scanning techniques (e.g. e-beam and ion beam), have a limited throughput because they are serial processes. Nevertheless, recent studies employing a large number of probe tips have demonstrated the practicality of higher throughput processing [74, 106, 115–121]. For example, Mirkin and co-workers designed and fabricated a 55,000-pen 2D array, with a pen spacing of 90 and 20 μm in the *x* and *y* directions, respectively, occupying an area of 1 cm^2 [115, 118]. With this parallel approach, they constructed a 2D array

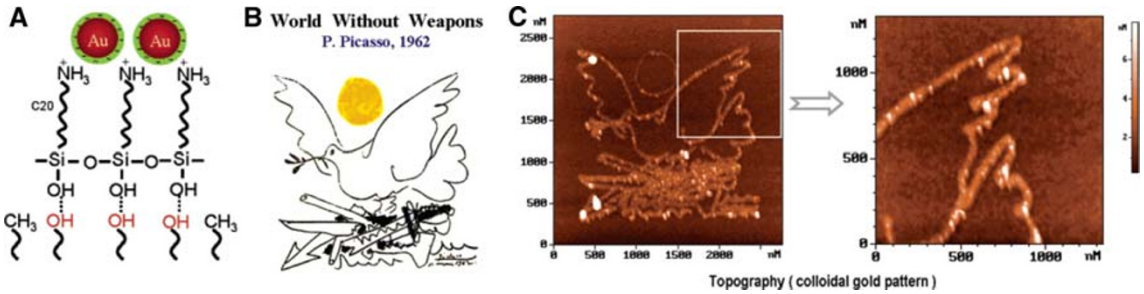

Fig. 7 Fabrication of a nanoarchitecture made of 2–6 nm Au nanoparticles selectively attached onto patterned SAMs. (**A**) Schematic of Au nanoparticle/SAMs structure created by AFM inscription, further functionalization of inscribed SAMs pattern with NTS, and selective attachment of Au nanoparticles. (**B**) The poster, entitled "World Without Weapons", created by Picasso in 1962. This was translated into an input signal to the conducting AFM tip that inscribes (contact mode, line width ~30 nm) a corresponding pattern on the top surface of OTS/Si monolayer specimen. (**C**) AFM topography image after 2–6 nm Au nanoparticles were deposited on amine terminated SAMs pattern, showing nanoscale replica of the poster made of nanoparticles/SAMs. (Reprinted with permission from Reference [91]. Copyright 2004 American Chemical Society.)

composed of 88 million gold dots on silicon wafer [115]. A massive array of phospholipids has been constructed as well with a lateral resolution of ~100 nm and a throughput of 5 cm^2/min [118].

Placement Using Electrostatic Templates

Electrostatic interactions between a charged substrate surface and nanoscale building blocks can be utilized for controlled placement. This is done by creating charge patterns, i.e. electrostatic templates, on the substrate surface and letting the building blocks interact with the charge patterns. Electret materials such as poly(methylmethacrylate) (PMMA), poly(tetrafluoroethylene) (PTFE), silicon dioxide, and silicon nitride can hold trapped charges or polarization for a long time, and charge patterns can be created on the electret film through direct injection of electrons, holes, or ions [122–128]. Several methods have been developed to locally charge the electret surface and then place the building blocks selectively on the charged areas. These include methods using electrical microcontact printing (e-μCP), electron beams, ion beams, and scanning probe microscopes such as AFM. These techniques will be reviewed one by one.

Creating Charge Patterns Using Electrical Microcontact Printing (e-μCP)

Jacobs and Whitesides have developed a method, called electrical microcontact printing (e-μCP), wherein charge patterns are created in a thin electret film in parallel processing by injecting charges via a flexible metal electrode in contact with the electret surface [122]. Figure 8 illustrates the concept of e-μCP. A patterned stamp made of polydimethylsiloxane (PDMS) is coated with a thin Au/Cr layer and is brought into contact with a thin PMMA film (80 nm) on doped silicon wafer, Fig. 8A and B. A voltage pulse is applied between the Au/Cr layer on the PDMS stamp and the conductive silicon wafer, Fig. 8B. The PDMS stamp is removed and the PMMA electret retains charges (positive or negative depending on the polarity of voltage pulse) in patterns which replicate the patterns on the PDMS stamp, Fig. 8C. Using this method, they made patterns of trapped charges at a resolution better than 150 nm in less than 20 s for areas as large as 1 cm^2. Selective placement of 500 nm–20 μm particles onto the micrometer scale charged patterns on PMMA film was demonstrated.

The e-μCP method was extended to the nanoscale through improved electrode design that enabled higher resolution charge transfer to PMMA electret. Barry et al. was able to place 5–40 nm sized nanoparticles from gas phase onto a PMMA surface in shapes of lines and squares with 60 nm lateral resolution [129]. This was accomplished using a flexible thin Si electrode that was patterned by phase-shift photolithography and reactive-ion etching, to produce line widths as small as 50 nm. Another approach to higher resolution charge transfer has recently been introduced by Whitesides and co-workers [130]. This method utilizes the nanotransfer printing (nTP) developed by Rogers and co-workers [131] and produces narrow (10–40 nm) metal lines only along the edges of raised features of the PDMS stamp. When e-μCP is used to transfer charges through these thin metal lines, the area of charge transfer is greatly reduced as can be seen in the KFM (Kelvin probe force microscopy [132]) images shown in Fig. 9A and B. Figure 9C and D show SEM images after 200 nm solfonate-modified PS spheres were selectively adsorbed on charged patterns shown in Fig. 9A and B,

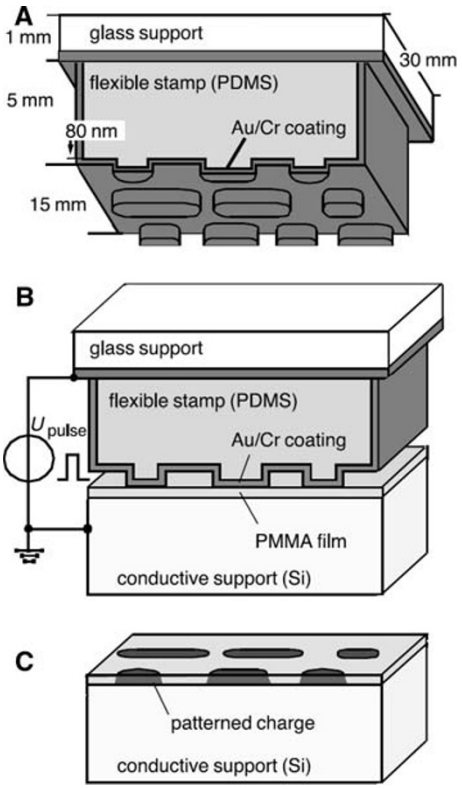

Fig. 8 Principle of electrical microcontact printing (e-μCP). (**A**) The flexible, metal-coated stamp is placed on top of a thin film of PMMA supported on a doped, electrically conducting Si wafer. (**B**) An external voltage is applied between the Au and the Si to write the pattern of the stamp into the electret. (**C**) The stamp is removed; the PMMA is left with a patterned electrostatic potential. (Reprinted with permission from Reference [122]. Copyright 2001 American Association for the Advancement of Science.)

respectively. The nanoparticles placed on the size-reduction pattern, i.e. the pattern in Fig. 9B, yielded structures only one particle across, Fig. 9D.

Creating Charge Patterns Using Electron Beams

Electron beam irradiation also can create charge patterns on the electret material. Although electron beam irradiation is a serial process and, therefore, slow, charge patterns can be generated with enhanced speed if a low dose electron beam is used. Joo et al. demonstrated fast charge patterning employing a low dose electron beam, which was followed by deposition of positively charged silver nanoparticles via an electrospray technique [133]. The charged nanoparticles were selectively deposited onto a charge pattern on PMMA with a lateral resolution of 0.7 μm, Fig. 10. Since the dose they used for charge patterning on PMMA was very low (50 nC/cm^2), several orders of magnitude lower than typical e-beam resist dose, this approach holds potential for controlled placement of nanoscale building blocks for a large area in a reasonably short time.

Controlled placement of biological molecules, such as DNA and proteins, was made by exploiting electron beam induced charge trapping [127, 134]. For example, by selecting an appropriate electron beam irradiation energy on glass substrate, Chen and co-workers created a layer (5–20 nm) of highly localized *positive* charges at the irradiated spot even though the net charge in the region as a whole was negative [134]. This effect was due to the escape of secondary electrons, which varies with the incident electron beam energy [135, 136]. When the glass substrate with positively charged pattern was immersed in the DNA solution, the DNA, which are negatively charged, were selectively attracted onto the positively charged area. Using this procedure, they demonstrated the placement of DNA on a glass substrate with lateral resolution of $\sim$50 nm.

Creating Charge Patterns Using Ion Beams

Ion beams are also used as charge sources for creating patterns on electret films. Once the charged pattern is produced, oppositely charged nanoscale building blocks can be selectively adsorbed by immersing in a colloid containing charged particles, spraying the building blocks from the gas phases, or attracting them from the solid state powder form. For example, Fudouzi et al. used a Ga^+-focused ion beam (FIB) to draw a charge pattern on a $CaTiO_3$ substrate [137]. They made a charged dot array (dot diameter: $\sim$6 μm), with the electric field from the charged dots being controlled by the Ga^+ ion dose. Using an appropriate ion dose and choosing appropriate size microspheres (10 μm polymer spheres), they were able to place only one particle onto each charged dot. They attributed this one-particle-per-dot deposition to the shielding effect: once one particle occupies a charged dot, it shields the electric field coming from the charged dot, reducing the effective electric field.

Creating Charge Patterns Using AFM

Atomic force microcopy (AFM) offers another way to deposit localized charges on electret films [124, 125, 138, 139]. In this approach, a conducting AFM tip is positioned on the surface of a thin electret film which is deposited on a conducting substrate. When voltage pulses are applied between the conducting AFM tip and the substrate, localized charges can be deposited in the electret film. Depending on the polarity of the voltage pulses, either positive or negative charges can be deposited. This is a

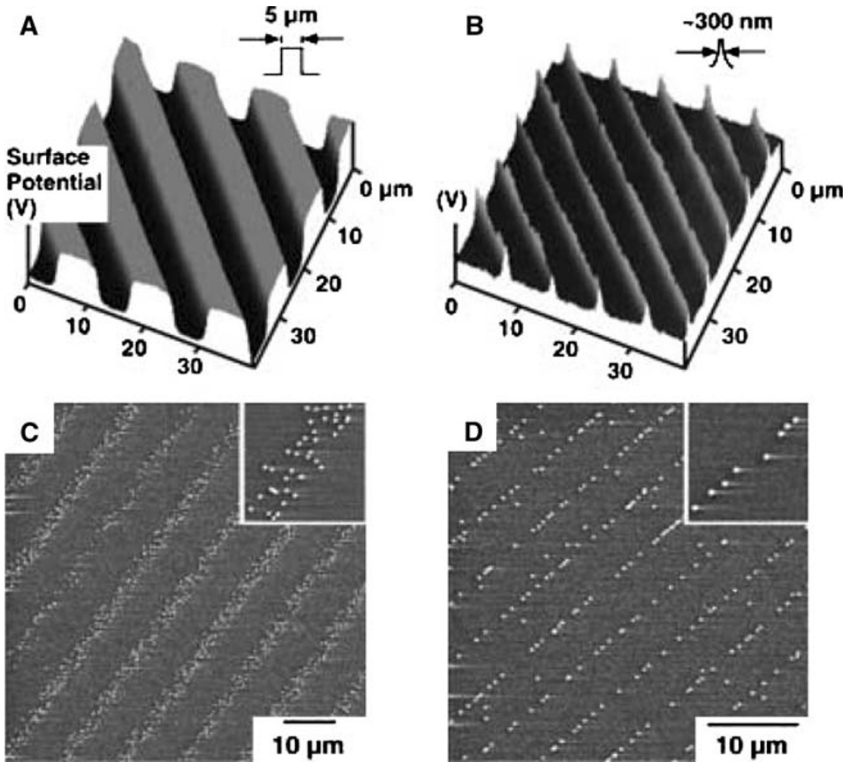

Fig. 9 Size-reduction of charge transfer area exploiting nTP and its application to nanoparticle placement. (**A**–**B**) KFM (Kelvin probe force microscopy [132]) images obtained from the e-μCP of metal-coated PDMS stamps without using nTP (**A**) and with using nTP (**B**). (**C**–**D**) SEM images of nanoparticle adsorption over the pattern of charge shown in (**A**) and (**B**), respectively. The nanoparticles are 200 nm sulfonate-modified PS spheres. The size-reduction pattern, (**D**), yields structures only one particle across. (Reprinted with permission from Reference [130]. Copyright 2005 Wiley-VCH.)

very attractive feature of AFM assisted patterning since it can create a combination of positively and negatively charged patterns on a same substrate by just varying the voltage pulse polarity. The amount of charge deposited and the area of the localized charge can be controlled by varying the height of the voltage pulses; with increasing pulse height, the amount of deposited charge and charged area increases [138]. The charge area also depends on the tip geometry and quality. With their best tips, Mesquida and Stemmer obtained a lateral resolution of $\sim$100 nm using poly(tetrafluoroethylene) (PTFE) as an electret, as verified by the surface potential image acquired with KFM [138]. On the charge patterns created with AFM, they were able to selectively deposit 290 and 50 nm silica beads.

With AFM under high-vacuum conditions ($\sim 1 \times 10^{-6}$ Torr) and using a layered structure, $Si_3N_4/SiO_2/Si$ (NOS), as an electret film, Gwo and co-workers were able to write charge patterns with a lateral resolution of $\sim$30 nm [139]. Figure 11A shows a schematic of their experimental setup for writing and sensing charge patterns with nanoscale resolution. Figure 11B and C show KFM images demonstrating the capability of patterning with a minimum feature size of $\sim$30 nm. The darker and brighter regions correspond to electron and hole injections, respectively. If one charged dot is used as one bit in the application of a charge storage device, this lateral resolution corresponds to $\sim$500 Gbit/in^2. The charge patterns can serve as electrostatic templates onto which charged nanoscale building

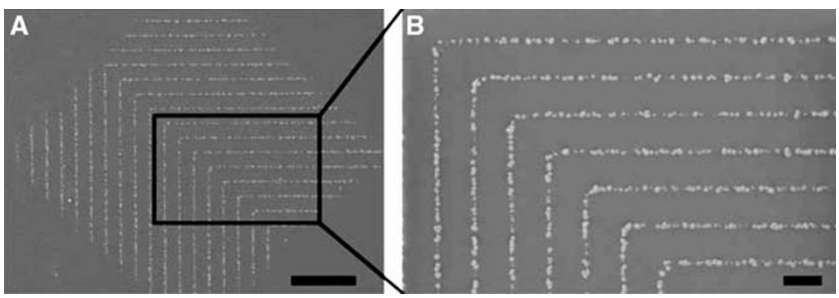

Fig. 10 SEM images after positively charged silver nanoparticles were sprayed onto the negatively charged e-beam pattern. About 0.7 μm thick lines were generated over a large area with doses as low as 50 nC/cm^2, showing the feasibility of ultrafast patterning by electrostatic lithography. (**A**) Scale bar = 50 μm. (**B**) Scale bar = 10 μm. (Reprinted with permission from Reference [133]. Copyright 2006 AVS The Science & Technology Society.)

blocks can be selectively adsorbed. Figure 12 shows controlled placement of thiol-terminated 5 nm Au nanoparticles that are selectively adsorbed onto negatively charged line patterns with ~30 nm resolution.

DNA-Programmed Placement

DNA is a remarkable molecule that stores all the genetic information required for proper functioning and reproduction of living organisms. The important feature of DNA is the capability of molecular recognition through the Watson–Crick base paring, in which, through hydrogen bonding, Adenine (A) binds specifically to Thymine (T) and Guanine (G) to Cytosine (C). In addition, the DNA is a nanoscale molecule; for double-helical B-DNA, the diameter is about 2 nm and its helical pitch is about 3.4 nm [140–142]. The molecular recognition capability of DNA as well as its nanoscale dimension has been utilized as a powerful tool for programmed arrangement of various nanoscale building blocks. The key to this approach is to design DNA motifs that contain molecular recognition parts which can specifically combine with other DNA motifs in a selective and programmable manner. Conjugating nanoscale building blocks such as nanoparticles, proteins, ions, and organic/inorganic molecules with the DNA motifs can lead to the well-defined arrangement of nanoscale building blocks. This DNA-programmed assembly of nanoscale building blocks is a fascinating emerging field with high potential for bottom-up construction of nanoscale devices and sensors. Here we present several examples of recent successful studies. The interested reader may also look at excellent reviews and the references therein [140–150]. In this section, we first introduce DNA-assisted assembly using single-stranded DNA (ss-DNA), which leads to formation of *linear* arrays of nanoscale building blocks. We then briefly describe the key aspects of artificial DNA motifs (DNA tiles), which are more rigid than ordinary DNA, can be assembled into *crystals*, and are suitable as scaffolding for nanoscale building blocks. We then review programmed assembly of nanoscale building blocks that utilize DNA crystals as scaffolds. Several successful studies will be presented as examples.

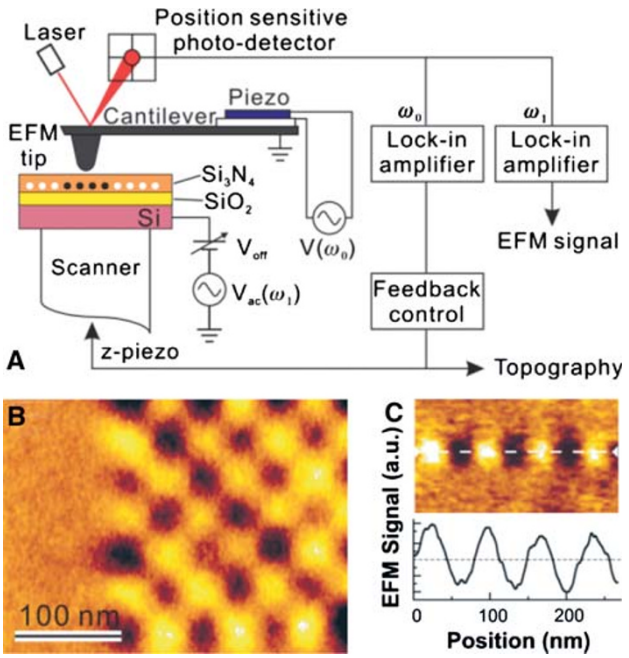

Fig. 11 Charge writing and sensing with nanoscale resolution. (**A**) Schematic of the experimental setup. (**B**) KFM images of high areal density (~500 Gbit/in^2) charge bits injected into an NOS (30 Å Si_3N_4/22Å SiO_2/Si) ultrathin film. The darker and brighter regions were injected with electrons and holes, respectively. (**C**) KFM image and cross-sectional KFM line profile of charge bits. (Reprinted with permission from Reference [139]. Copyright 2006 Wiley-VCH.)

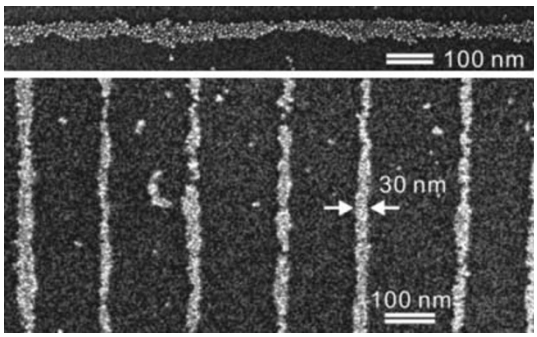

Fig. 12 SEM images of selectively adsorbed Au nanoparticles. The images show that thiol-terminated 5 nm Au nanoparticles can be selectively adsorbed onto negatively charged line patterns at a linewidth resolution of 30 nm. (Reprinted with permission from Reference [139]. Copyright 2006 Wiley-VCH.)

Because ss-DNA is topographically of one-dimension, it is natural to try to utilize it for assembly of linear arrays of nanoscale building blocks. Many studies over the last decade have demonstrated that this approach is successful. For example, Niemeyer et al. used DNA–protein conjugate motifs to form linear protein arrays [148, 151–153]. They first made STV–ssDNA (streptavidin–single-stranded DNA) conjugates through covalent coupling between STV and thiol terminated short ss-DNA. These STV–ssDNA motifs were then hybridized with a long ss-DNA that contains sections with sequences complementary to those of the short DNA in STV–ssDNA. This led to the programmed formation of a linear streptavidin array along the long ss-DNA. This approach is not limited to streptavidin, but can be applied to many nanoscale objects that can bind to ss-DNA. For example, Matsuura et al. demonstrated one-dimensional assembly of galactose [154], Waybright et al. showed the assembly of organometallic compound

arrays [155], and various nanoparticle arrays were also demonstrated by other groups [156–158].

For more complex assemblies in two- or three-dimensional forms, the ordinary DNA is not appropriate as a building unit because it is topographically one-dimensional and it is not mechanically stiff enough. However, artificial DNA has been designed and fabricated which is suitable for systematic and robust assembly of DNA arrays in two-, and three-dimension [140, 142, 147, 159–162]. The key to this approach, which was pioneered by Seeman, is to design DNA motifs or DNA "tiles" that are mechanically robust and contain molecular recognition parts, called sticky ends, which can specifically fit together with the complementary sticky ends of other DNA tiles, much like mating Lego pieces. (A sticky end is a short single-stranded DNA portion protruding from the end of double-stranded DNA [142]. A sticky end can combine with another sticky end only if their base sequences are complementary to each other, much like a key and lock fit together.) The artificial DNA motifs were made using a process called *reciprocal exchange*, in which two DNA strands are juxtaposed, nicked, and rejoined, leading to a crossover of the two original strands [147, 163]. Various robust artificial DNA motifs with programmed sticky ends have been made using reciprocal exchange. An example is shown in Fig. 13 where DNA double-crossover (DX) units were synthesized and used for construction of two-dimensional DNA arrays [142]. The DX units were made through two reciprocal exchanges between two double-stranded DNA molecules [147, 159, 163]. When two different DX molecules (A and B* in Fig. 13B) were linked together through complementary sticky ends, well-organized two-dimensional DNA arrays (2D DNA crystals) were made, Fig. 13C and D. Many other types of artificial DNA motifs were also synthesized. For example, DNA triple-crossover (TX) molecules were made in which three double-stranded DNA helices are linked together [147, 163, 164]. Using artificial DNA motifs as building tiles (having different sequences, sizes, and shapes), various two-dimensional DNA crystals have been assembled [161, 162, 164–168].

Programmable DNA tiles and their assembly into crystals can be exploited to construct arrays of various nanoscale building blocks. This has been accomplished by employing the DNA crystals as scaffolds onto which nanoscale building blocks systematically attach. This may be done either by post-attachment of the building blocks on the pre-existing DNA scaffolds or by pre-attachment of the building blocks to DNA tiles, forming DNA-building block conjugates, followed by the DNA-programmed assembly of the DNA-building block conjugates. Using these approaches, various building blocks were controllably assembled, including arrays of proteins [165, 167, 169–171] and nanoparticles [168, 171–173]. A few examples of these recent studies are presented below.

Yan, LaBean, and their co-workers demonstrated self-assembly of streptavidin arrays using DNA scaffolds [165]. They first designed and constructed DNA tiles that were made of four four-arm DNA branched junctions (4×4 DNA tiles), consisting of multiple DNA strands, pointing in four directions (north, south, east, and west in the tile plane). These 4×4 DNA tiles were self-assembled, through the Watson–Crick base paring at the sticky ends,

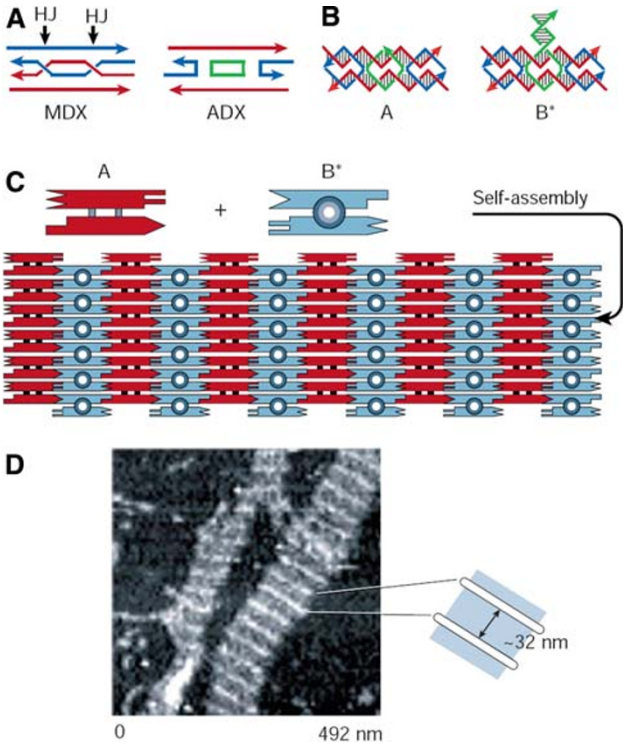

Fig. 13 Two-dimensional DNA arrays. (**A**) Schematic drawings of DNA double crossover (DX) units. In the meiotic DX recombination intermediate, labeled MDX, a pair of homologous chromosomes, each consisting of two DNA strands, align and crossover in order to swap equivalent portions of genetic information; 'HJ' indicates the Holliday junctions. The structure of an analogue unit (ADX), used as a tiling unit in the construction of DNA two-dimensional arrays, comprises two red strands, two blue crossover strands and a central green crossover strand. (**B**) The strand structure and base pairing of the analogue ADX molecule, labeled A, and a variant, labeled B*. B* contains an extra DNA domain extending from the central green strand that, in practice, protrudes roughly perpendicular to the plane of the rest of the DX molecule. (**C**) Schematic representations of A and B* where the perpendicular domain of B* is represented as a blue circle. The complementary ends of the ADX molecules are represented as geometrical shapes to illustrate how they fit together when they self-assemble. The dimensions of the resulting tiles are about 4×16 nm and are joined together so that the B* protrusions lie about 32 nm apart. (**D**) The B* protrusions are visible as 'stripes' in tiled DNA arrays under an atomic force microscope. (Reprinted with permission from Reference [142]. Copyright 2003 Macmillan Publishers Ltd.)

into an array of nanogrids (schematic in Fig. 14A). The nanogrid array was then modified by incorporating a biotin group into the center of each 4×4 DNA tile. When streptavidin was added to the solution of the biotin-modified nanogrids array, the streptavidin combined with the biotin, resulting in a well-defined streptavidin nanoarray, Fig. 14.

Nanoparticle arrays were also constructed through DNA-programmed assembly. For example, Le et al. demonstrated programmed assembly of Au nanoparticles by hybridizing DNA-functionalized Au nanoparticles with pre-assembled 2D DNA scaffolds on a mica surface [173]. In their approach, they first designed and fabricated four distinct DNA double-crossover (DX) tiles (tile type: A, B, C, and D; dimension: ~ 2 nm $\times$ 4 nm $\times$ 16 nm) using 21 synthetic DNA strands. The DX tiles contained sticky ends whose sequences were designed such that they can self-assemble into a 2D DNA crystal (schematic in Fig. 15C) where each tile type forms a row and each row comes together in a repeated sequence of A, B, C, and D.

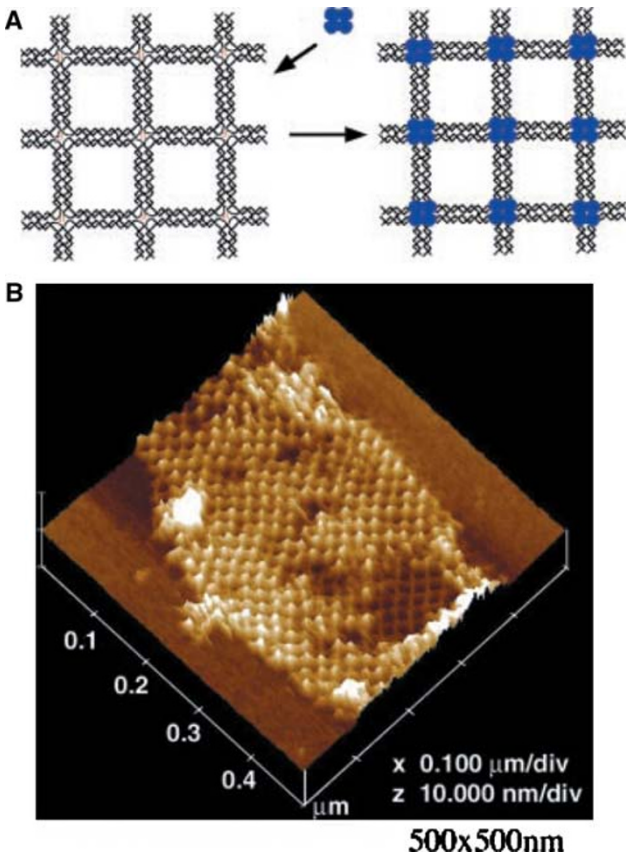

Fig. 14 Self-assembly of protein arrays templated by 4×4 DNA nanogrids. (**A**) Schematic drawing of the DNA nanogrids scaffolded assembly of streptavidin. (Left) The DNA nanogrids, a biotin group is incorporated into one of the loops at the center of each tile. (Right) Binding of streptavidin (represented by a blue tetramer) to biotin will lead to protein nanoarrays on DNA lattices. (**B**) AFM image of the self-assembled protein arrays. (Reprinted with permission from Reference [165]. Copyright 2003 American Association for the Advancement of Science.)

In Fig. 15C, the DX tile B (red) contained an extended single-stranded DNA feature onto which a DNA–Au nanocomponent was able to bind. The DNA–Au nanocomponents were separately prepared by functionalizing 5 nm Au nanoparticles with thiolated single-stranded DNA via well-known thiolate-Au conjugation [69]. When a droplet containing DNA–Au nanocomponents was deposited onto a pre-assembled 2D DNA crystal, the DNA–Au nanocomponents were selectively attached to DX tile B's via DNA hybridization, leading to self-assembly of 5 nm Au nanoparticles as evidenced by AFM and TEM images in Fig. 15A and B, respectively.

The 2D DNA crystal architecture composed of four tiles A, B, C, and D (called an ABCD tile array, like the one in Fig. 15C) has been utilized for construction of 2D arrays of other nanoscale entities. For example, Williams et al. demonstrated assemblies of 2D peptide arrays and 2D peptide–antibody arrays, Fig. 16 [169]. They used the four DNA tiles described above, except that tile B did not contain an ss-DNA extension, but tile D contained two extensions of DNA capture probes. The DNA capture probe (schematic in Fig. 16A) is a ss-DNA designed to capture a myc-peptide fusion, a conjugate formed by covalent linking between a ss-DNA and a myc-peptide. The sequence of ss-DNA in the myc-peptide fusion is complementary to that of the DNA capture probe, leading to a programmed binding between them, Fig. 16B. An anti-myc antibody can then bind to an myc-peptide through peptide–antibody interaction, Fig. 16 C. Figure 16D–F show AFM images of sequential construction of 2D arrays, starting from the formation of a DNA crystal (Fig. 16D), an array of the myc-peptides (Fig. 16E), and an array of peptide–antibody conjugates (Fig. 16F). The AFM height profiles in Figs. 16G–I show the step-by-step increase of the heights due to the capture of the myc-peptide fusions and subsequent binding of the anti-myc antibodies to the myc-peptides.

Previous examples demonstrate assembly of nanoscale building block arrays that were made through *post*-placement of building blocks onto *pre*-assembled DNA crystal scaffolds. An alternative scheme is to prepare ss-DNA-building block conjugates first, followed by incorporation of the conjugates into DNA tiles and eventually into a DNA crystal. This leads to programmed placement of nanoscale building blocks onto specific sites in a DNA crystal. For example, Xiao et al. demonstrated self-assembly of metallic nanoparticle arrays using ss-DNA–nanoparticle conjugates [174]. They designed 22 different types of ss-DNA which form four types of DX tiles (referred to A, B, C, and D). Au nanoparticles of 1.4 nm in diameter were used to form DNA–nanoparticle conjugates

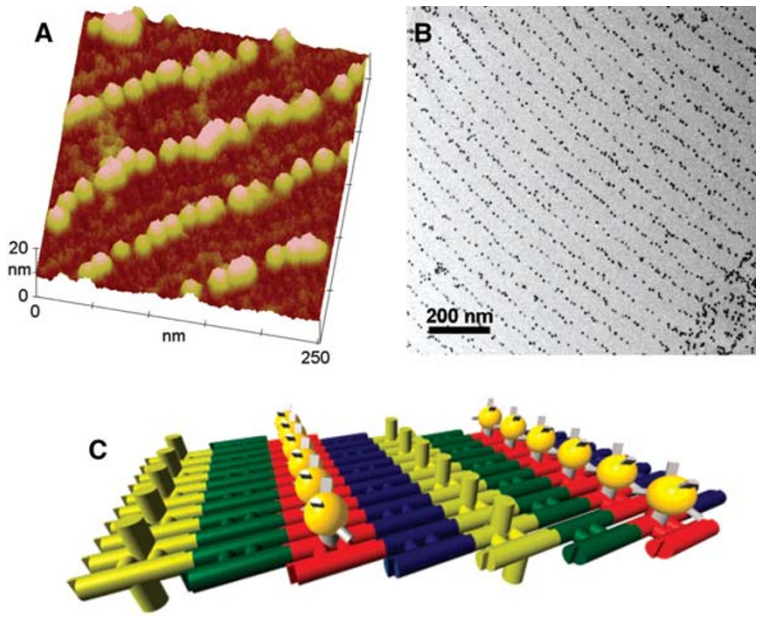

Fig. 15 Visualization of the DNA–Au nanocomponent arrays. (**A**) Topographical AFM image of an assembled array providing a 3D visualization of the assembled DNA–Au nanocomponents, DNA marker rows, and DNA scaffolding. (**B**) TEM image of the nanocomponent array. The high-contrast particles in the image measure 6.2 ± 0.8 nm in diameter. (**C**) Schematic of DNA–Au nanocomponent arrays. DX tile color: blue, red, green, and yellow for DX tiles A, B, C, and D, respectively. DX tile B (red) contains an extended single-stranded DNA feature that hybridizes to complementary single-stranded DNA in the DNA–Au nanocomponent. DX tile D (yellow) includes extended structures composed of DNA hairpins above and below the crystal plane, which are used as topographical markers on the DNA crystal. (Reprinted with permission from Reference [173]. Copyright 2004 American Chemical Society.)

through covalent bonding between the Au nanoparticles and one type of ss-DNA which was modified with a thiol. These conjugates were then specifically incorporated into tile B during tile formation. When the DNA tiles self-assembled to a 2D DNA crystal, a 2D Au nanoparticle array having programmed nanoscale separations (4 and 64 nm in x and y direction, respectively) was constructed. Other examples include recent demonstration of programmed assembly of 5 and 10 nm Au nanoparticles into a 2D rhombic pattern by Zheng et al. [168]. They designed and constructed triangular DNA motifs (termed 3D DX triangles) that were composed of three DX molecules forming a triangle. For each motif (3D DX triangle), two DX molecules were designed to form a rhombic DNA crystal, with one remaining DX molecule being used for attachment of a 5 or 10 nm Au nanoparticle. Self-assembly of the 3D DX triangles into a DNA crystal led to a formation of a precisely positioned nanoparticle array in rhombic pattern.

Placement Using Dielectrophoresis

Dielectrophoresis is the movement of uncharged objects in a liquid dielectric medium under the influence of a non-uniform electric field [175]. Dielectrophoresis originates from the induced dipole moment of an object, whose value depends on the dielectric and electrical properties of both the object and the surrounding medium. With an appropriate design of the non-uniformity of the electric field, the movement of an object can be manipulated, allowing controlled placement onto specific locations and/or alignment in a particular direction. Dielectrophoresis has been extensively studied as a promising tool for manipulating various nanoscale or microscale objects such as nanowires, carbon nanotubes, nanoparticles, DNA, proteins, cells, bacteria, and viruses [176–188]. Recently, a lot of effort has been made to utilize dielectrophoresis for controlled placement/alignment of nanoscale building blocks for fabrication of nanoelectronic devices or sensors, where precise placement of the building blocks onto addressable locations is required on a large scale. A brief review of these advances is given here.

The dielectrophoretic force is governed by many factors; the complex dielectric constant of an object and that of surrounding medium, the geometry of the object, the magnitude and frequency of the applied electric field, and the spatial distribution of the electric field. For an AC bias, the time-average dielectrophoretic force on a cylindrical object with diameter r and length l, $\langle F \rangle$, is given by [189–191]

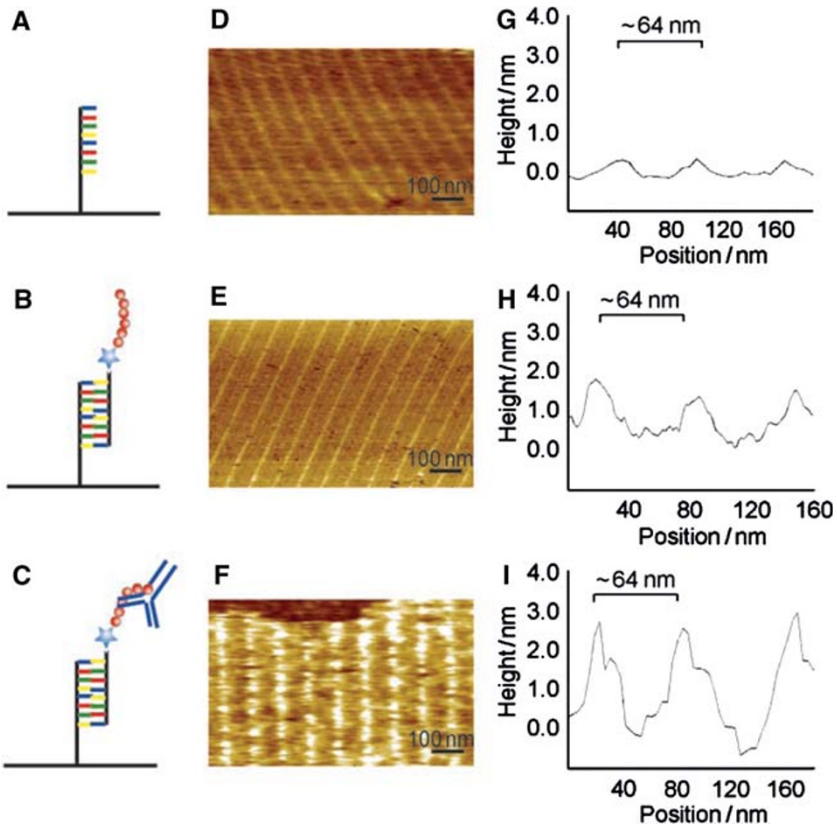

Fig. 16 AFM imaging of the peptide nanoarrays. (**A–C**) Schematic illustration showing the DNA capture probe on the DNA surface, annealed to the myc-peptide fusion, and immunocaptured by the anti-myc antibody, respectively. (**D–F**) AFM images were collected for the array before hybridization of the myc-peptide fusion, after hybridization of the myc peptide, and following incubation with the anti-myc antibody, respectively. (**G–I**) Height profiles were determined for the array, the array displaying the myc-peptide epitope, and the array with the anti-myc antibody bound to the myc epitope, respectively. (Reprinted with permission from Reference [169]. Copyright 2007 Wiley-VCH.)

$$\langle \mathrm{F} \rangle = \frac{1}{2}\pi r^2 l \varepsilon_{\mathrm{m}} \mathrm{Re}\{\mathrm{K}(\omega)\} \nabla |E_{\mathrm{rms}}|^2, \quad (1)$$

where

$$K(\omega) = (\varepsilon^*_{\mathrm{obj}} - \varepsilon^*_{\mathrm{m}})/\varepsilon^*_{\mathrm{m}} . \quad (2)$$

E_{rms} is the root mean square value of the electric field and ε_{m} is the dielectric constant of the medium. $\varepsilon^*_{\mathrm{obj}}$ and $\varepsilon^*_{\mathrm{m}}$ are complex dielectric constants for the object and the medium, respectively. The complex dielectric constant ε^* is a function of bias frequency ω, dielectric constant ε, and conductivity σ, and is given by

$$\varepsilon^* = \varepsilon - i\sigma/\omega. \quad (3)$$

Equations 1–3 provide the fundamental basis for controlling the dielectrophoretic forces exerted on the objects. With appropriate choice of parameters (electric field gradient, frequency, dielectric medium, etc.), controlled placement and/or alignment of nanoscale and microscale building blocks have been accomplished.

Using AC bias with frequency above 1 MHz, Nagahara et al. was able to place single-walled carbon nanotubes (SWNTs) between two metal electrodes separated by a few tens of nanometers [178]. In addition, they found that when high frequency (>1 MHz) AC bias was used, very few contaminants were attached to the substrate although the aqueous SWNT solution generally contains a lot of impurities such as amorphous carbons. They attributed this selective placement of SWNTs over contaminants to the influence of frequency on the dielectrophoretic forces as expressed in the Eqs. 1–3; at higher frequencies, the $K(\omega)$ (therefore $\langle F \rangle$) is proportional to the dielectric constant difference, $\varepsilon_{\mathrm{obj}} - \varepsilon_{\mathrm{m}}$. If the difference is larger for SWNTs, then the dielectrophoretic force $\langle F \rangle$ for SWNTs would be larger than that for the contaminants, leading to selective attraction of SWNTs. In addition, under AC bias, the time-averaged force exerted on any charged objects becomes zero and no effective attractive forces are applied to the charged impurities. Their observation was in agreement with results from other groups [180, 192]. For example, Chen and co-workers studied the effect of the frequency of AC bias on the alignment of SWNTs [192]. They observed increasing SWNTs alignment and decreasing contaminants as frequency was increased from 0 (DC) to 5 MHz. Krupke and co-workers reported excellent and reproducible alignment of single carbon nanotube bundles with AC frequency over 1 kHz, Fig. 17 [180]. Similar studies have been carried out for nanowires of various materials including Au, Ag, GaN, SnO_2, Ga_2O_3, CdSe, and SiC [188, 190, 191, 193].

Beyond the capability of positioning carbon nanotubes or nanowires between electrode pairs, for practical

realization of nanoscale devices and sensors, more challenging requirements must be met. First, every electrode pair should be bridged by only a single nanotube/nanowire. Second, positioning of single nanotubes/nanowires over electrode pairs should be done simultaneously over a large area in parallel processing. A lot of effort, and with significant progress, has been made to meet these challenges over the past few years. For example, Chung et al. explored placing multi-walled carbon nanotubes (MWNTs) between a pair of opposing electrodes separated by a gap [179]. They studied the effect of combining DC and AC electric fields on positioning of MWNTs and found that the ratio of DC versus AC field affects the degree of alignment, the separation between adjacent MWNTs deposited between electrodes, and the degree of contaminant deposition. With an appropriate electrode design and an optimized DC/AC ratio (AC frequency fixed at 5 MHz), they were able to place a *single* MWCT onto each electrode pair with a 90% yield as demonstrated for an array of 100 electrode pairs. They attributed this controlled placement of single MWNTs to a combined result of a dielectrophoretic force, an electrophoretic force, and a mechanical flow of ions generated by electrokinetic force. Upon bridging of an electrode pair by a single MWNT, these forces dramatically change and prevent the approach of other MWNTs, leading to single MWNT placement per electrode pair.

Krupke and co-workers utilized dielectrophoretic forces for simultaneous and site-selective placement of single bundles of SWNTs onto an array of electrode pairs [177]. With AC bias, typically $V_{p\text{-}p} = 1$ V and frequency at 1 MHz, they showed that $\sim$70% of the electrode pairs were bridged by SWNT bundles, of which more than 50% were by single bundles. This self-limiting positioning of single bundles was attributed to the change of electric field upon bridging of an electrode pair [194]. An additional important finding of this study is that only metallic or quasi-metallic SWNTs were attracted to the electrodes, whereas semiconducting SWNTs were repelled. This was attributed to the fact that at high AC frequency the dielectrophoretic force is proportional to the difference of dielectric constants of carbon nanotubes and solvent medium, $\varepsilon_{CNT} - \varepsilon_m$, where ε_{CNT} is the dielectric constant of nanotubes and ε_m that of the solvent medium (see Eqs. 1–3). They used *N,N*-dimethylformamide (DMF) as solvent, whose dielectric constant ε_m is 39. At the 1 MHz frequency they used, the dielectric constant ε_{CNT} for metallic SWNTs is much larger than 39, whereas it is less than 5 for semiconducting SWNTs [195]. This led to the attraction of metallic SWNTs to the electrodes, but repulsion of semiconducting SWNTs from the electrodes. Combined with a technique to well disperse individual SWNTs [196], this capability of dielectrophoretic forces to selectively position metallic SWNTs was exploited to separate metallic SWNTs from the usual mixture of metallic and semiconducting SWNTs [176].

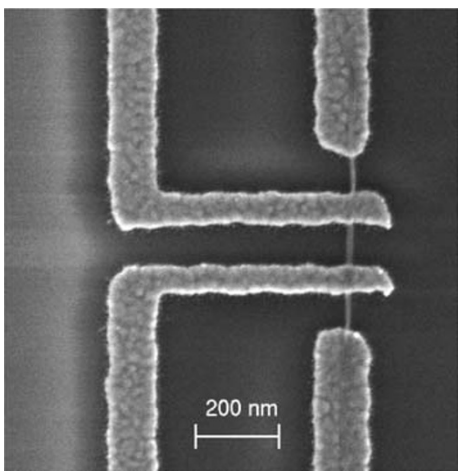

Fig. 17 Scanning electron micrograph of a single bundle of carbon nanotubes trapped on four Au electrodes. The alternating electric field has been generated between the *upper right* and *lower right* electrodes. The other two electrodes were at floating potential. The bundle diameter is 9 nm. (Reprinted with permission from Reference [180]. Copyright 2003 Springer.)

A significant advance was made recently for directed positioning of carbon nanotubes. Using AC dielectrophoresis and systematic electrode design, Krupke and co-workers were able to position single SWNTs across electrode pairs over a large area with more than 90% yield [194]. The density of the SWNT arrays was also very high, in the order of 3–4 million SWNTs per cm^2. This high density was possible due to the systematic design of electrodes (along with an appropriate choice of gate oxide thickness), where the biasing electrodes were all connected to one AC source, while counter electrodes were floated and capacitively coupled to a gate electrode. Most of the electrode pairs were bridged by a single SWNT or a single nanotube bundle. Figure 18A shows a representative image of the whole array, where each of the five adjacent electrode pairs was connected by exactly one nanotube. This was attributed to the self-limiting behavior in nanotube bridging: when a nanotube assembles into an electrode pair and makes electrical contact with the two electrodes, the dielectrophoretic force fields change incisively, preventing other nanotubes from approaching. They performed numerical simulations of the dielectrophoretic forces using the finite element method (FEM). Figure 19B, D and A, C compare ∇E^2, hence the dielectrophoretic forces $\langle F \rangle$ (see Eq. 1), with and without the presence of a nanotube bridging two electrodes, respectively. In the absence of nanotubes, the dielectrophoretic forces are attractive in all regions, while the forces become repulsive between electrodes when a nanotube bridges the electrodes.

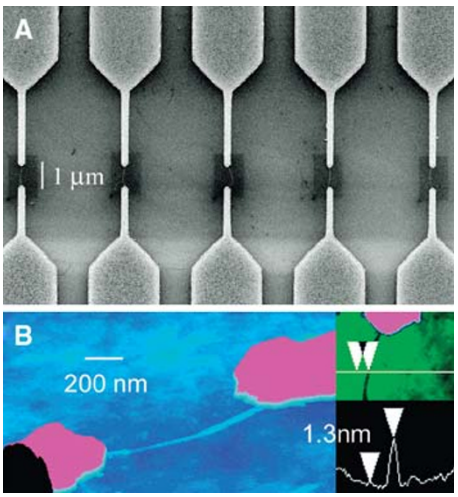

Fig. 18 (**A**) Zoom-in of the electrode array showing five adjacent devices, with each electrode pair bridged by one carbon nanotube, visible as fine white lines within the dark central areas. The dark areas are due to contrast enhancement while scanning the zoomed-in area around each device. (**B**) Atomic force microscopy image of one such device. The height profile confirms the bridging by an individual nanotube. (Reprinted with permission from Reference [194]. Copyright 2007 American Chemical Society.)

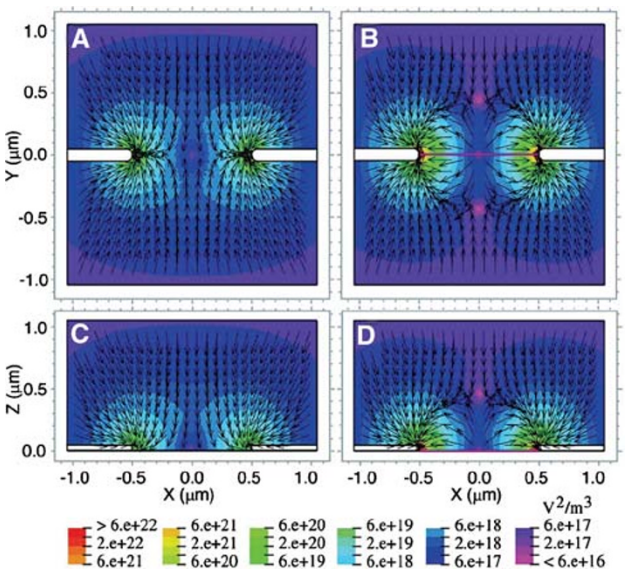

Fig. 19 Simulation of dielectrophoretic force fields. Simulated map of ∇E^2 in a volume around the electrodes for two orthogonal cross-sections. (**A**, **B**) ∇E^2 at the surface of the substrate (X–Y plane at $Z = 0$). (**C**, **D**) ∇E^2 perpendicular to the substrate (X–Z plane at $Y = 0$). The arrows indicate the direction of the force acting on a highly polarizable nanotube–surfactant hybrid and, hence, the direction of nanotube motion. The background color is the magnitude of ∇E^2. The dielectrophoretic force is attractive in all regions in the absence of deposited nanotubes (**A**, **C**), while the force becomes repulsive between the electrodes, once a nanotube (magenta line) has been deposited (**B**, **D**). (Reprinted with permission from Reference [194]. Copyright 2007 American Chemical Society.)

As we briefly discussed, dielectrophoresis is emerging as a powerful tool to manipulate and position individual nanoscale objects, especially one-dimensional entities such as nanowires and carbon nanotubes. In particular, the capability of self-limiting deposition and that of large area positioning in parallel processing are important characteristics of this method, making it a candidate for practical fabrication of nanoelectronic devices or sensors.

Non-close-packed (ncp) Patterns of Spherical Particles

Self-assembly of nanoscale and microscale spherical particles into two-dimensional ordered form has been extensively explored by many researchers exploiting capillary forces, spin coating, and controlled solvent evaporation [16, 197–203]. In these types of self-assembly, the structure is usually limited to the hexagonal close-packed (hcp) structure. For many applications, it is desirable to have non-close-packed (ncp) arrays. Yang and co-workers have developed a method which can form ncp arrays of colloidal spheres by controllably deforming the substrates supporting the spheres [204, 205]. In their approach, they first fabricated a three-dimensional hcp array of silica spheres via controlled solvent evaporation of a silica suspension. Then, by using lift-up soft lithography, a top single layer of hcp spheres was transferred to the surface of a PDMS film. This PDMS film was subsequently swollen with a solution of toluene in acetone, transforming the hcp array of silica spheres on the PDMS surface into a ncp array. The lattice spacing of this ncp array was readily tuned by varying toluene concentration. A ~50% increase in the lattice spacing was demonstrated using pure toluene. Finally, using the μCP (micro contact printing) technique, the two-dimensional ncp array of silica spheres on the deformed PDMS film was then transferred to the surface of a substrate that was spin-coated with a thin film of poly(vinyl alcohol) (PVA), producing an ncp array on the PVA-coated substrate.

In another approach, ncp arrays with lattice structures other than hexagonal were obtained by mechanically stretching the sphere-coated PDMS elastomers instead of swelling. Figure 20A shows a schematic of this approach and Fig. 20B shows an example where a square ncp array of spheres was obtained by stretching the PDMS film along one direction (y-direction) while maintaining the length in the orthogonal direction (x-direction). An array of parallel lines was formed by stretching the PDMS film in the x-direction, Fig. 20A and C. Using a patterned PDMS stamp and stretching, patterned ncp arrays of spheres were also generated, Fig. 20D. These ncp arrays of colloidal spheres may find application in areas such as optics, photonics, surface patterning, and growth templates [20, 201, 202].

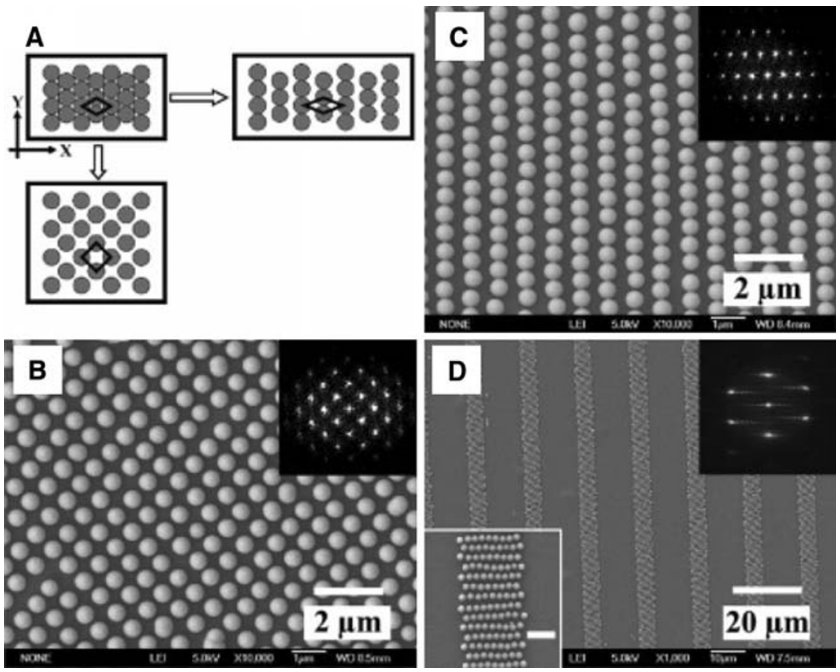

Fig. 20 (**A**) A schematic illustration of the 2D ncp sphere arrays with new crystal lattices formed by stretching the PDMS film along one direction while maintaining the length in the orthogonal direction; SEM images of 2D ncp arrays on PVA-coated substrates with (**B**) square lattice, (**C**) parallel single sphere-wires; and (**D**) ordered array of parallel lines of the 2D ncp array. Insets in the right display the corresponding FFT images. A high magnified view of (**D**) is shown in the left inset (the scale bar is 2 μm). (Reprinted with permission from Reference [204]. Copyright 2005 American Chemical Society.)

Möller and co-workers utilized micellar block copolymers to generate ncp arrays of metal and metal-oxide nanoparticles [203]. In this approach, they first generated polymeric micelles by dissolving poly(styrene)-*block*-poly(2-vinylpyridine) (PS-*b*-P2VP) block copolymers in toluene, Fig. 21. When metal precursors, such as $HAuCl_4$, were added, the metal ions were reduced at the micelle cores in such a way that exactly one elemental or oxidic particle was formed in each micelle, Fig. 21. A close-packed monolayer hexagonal array of the micelles was then formed by dipping a substrate into a dilute solution of the micelles (velocity: 40 mm/min) and pulling it out of the solution (velocity: 10 mm/min). Then the polymers wrapping the nanoparticles were removed using oxygen plasma, resulting in an ncp array of nanoparticles. Figure 22A is an AFM image in which a monolayer of close-packed micelle arrays was formed on a glass substrate from a PS(1700)-*b*-P[2VP($HAuCl_4$)$_{0.3}$(450)] solution. In this AFM image, the bright spots are from the elevations where the Au nanoparticles are located at the center of each micelle. After the polymers were removed by oxygen plasma (as can be seen from the height reduction from 35 nm to 8 nm in the AFM height profiles at the bottom of Fig. 22), an ncp array of gold nanoparticles was created, Fig. 22B. More importantly, this approach allowed the control of nanoparticle sizes as well as the interparticle spacing; the nanoparticle sizes were controlled between 1 nm and 15 nm by varying the concentration of metal precursors, and the interparticle distance was varied between 30 nm and 140 nm by using block copolymers with differing block lengths.

Focused Placement

For the various placement strategies discussed thus far, the placement precision is, at best, determined by the precision with which the templates (physical, molecular, or electrostatic) are defined on the substrate. Recently, there has been a lot of effort to develop new strategies that enable placement with much higher precision than the templates are defined [206]. These strategies have a common theme, which may be termed "focused placement", since the nanoscale building blocks are guided or focused onto targeted locations via electrostatic or mechanical forces. An analogy may be found in the operation of an electron microscope, where electron beam can be focused with sub-nanometer resolution although the guiding electromagnetic lenses are defined on the centimeter scale. In this section, we will review some recent advances in this approach including (1) electrostatic funneling, (2) directed assembly using molecular gradient patterns, (3) electrodynamic focusing of charged aerosols, and (4) guided placement

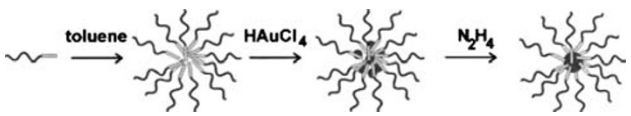

Fig. 21 Schematic drawing of the micelle formation of poly(styrene)-*block*-poly(2-vinylpyridine) (PS-*b*-P2VP) block copolymers in toluene. After complexation of $HAuCl_4$ to the pyridine units in the micellar core, the metal compound can be reduced to the zero-valent state by chemical conversion, leading to exactly one gold particle in each block copolymer micelle. (Reprinted with permission from Reference [203]. Copyright 2000 American Chemical Society.)

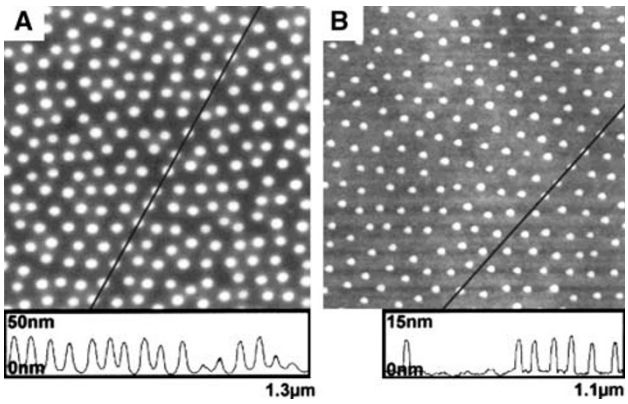

Fig. 22 (**A**) AFM topography image of a monomicellar film cast from a PS(1700)-*b*-P[2VP($HAuCl_4$)$_{0.3}$(450)] solution onto a glass substrate. The polymer micelles form a close-packed hexagonal array. (**B**) Same sample as in (**A**) but after the oxygen plasma treatment, resulting in naked Au particles on the glass substrate. The height profiles of the horizontal lines indicated in the images demonstrate the unchanged lateral periodicity of 90 nm after the plasma process and reduction of height to 8 nm, the height of the naked Au particles. (Reprinted with permission from Reference [203]. Copyright 2000 American Chemical Society.)

combining capillary effect and electrostatic forces. In addition, precision placement of nanoparticles utilizing polymer micelles via template-assisted placement will be presented. Although this scheme might not be considered as truly focused placement, we will discuss this approach in this section because the nanoparticle placement is confined to a small area in the center of a template, allowing precision placement using much coarser templates.

Electrostatic Funneling

One of the recently developed focused placement schemes utilizes long-range (>∼100 nm) electrostatic interactions between charged nanoscale building blocks and a charged surface in a solvent medium. In the approach developed by Koh and co-workers, named "electrostatic funneling", the substrate surface is charged with an appropriate combination of positively and negatively charged regions, and the combined electrostatic forces guide charged nanoparticles onto focused locations with nanoscale precision [82]. One example of the electrostatic funneling scheme is illustrated in Fig. 23, in which negatively charged nanoparticles are guided by a series of parallel lines that are functionalized alternatively with positively and negatively charged SAMs. This configuration produces maxima and minima in the interaction energy, creating a *gradient* in the interaction energy, Fig. 23A. The lateral forces generated by the interaction energy gradient push the charged nanoparticles onto the center region of the oppositely charged lines, where the interaction energy is minimum, resulting in the focused placement, Fig. 23B.

The effectiveness of electrostatic funneling has been demonstrated for a variety of geometries. Figure 24A shows an SEM image of Au nanoparticles (∼20 nm diameter) placed along the *center* of the silicon oxide lines (dark). The silicon oxide lines were functionalized with SAMs of (3-aminopropyl)triethoxysilane (APTES, $(C_2H_5O)_3$–Si–$(CH_2)_3$–NH_2), which were positively charged in aqueous solution [65, 69]. The bright lines are gold functionalized with 16-mercaptohexadecanoic acid (MHA, HS–$(CH_2)_{15}$–COOH), which were negatively charged in aqueous solution [65, 69]. The placement precision was as good as ∼5 nm as obtained from measuring the deviation of each nanoparticle from the centerline of the silicon oxide lines (from total 217 nanoparticles including all outliers). It is important to note that this nanometer scale precision was obtained over a large area even though the electrostatic guiding structure (silicon oxide and gold lines) was defined on a much coarser scale (line width ∼100 nm) using conventional CMOS fabrication processes.

This electrostatic funneling scheme works for other geometries as long as appropriate guiding structures are created. For example, when the guiding structures are

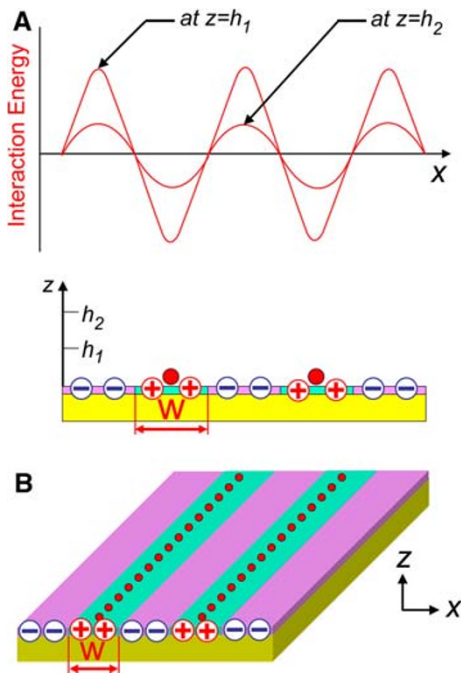

Fig. 23 Wafer-scale nanoparticle placement with electrostatic funneling. (**A**) A schematic of the electrostatic interaction energy in an aqueous solution for a negatively charged nanoparticle near a substrate surface functionalized with positively and negatively charged molecules. (**B**) The nanoparticles (red dots) are guided to the *centers* of positively charged lines (of width W ∼100 nm) where the interaction energy is minimum. (Reprinted with permission from Reference [82]. Copyright 2007 American Chemical Society.)

changed from lines to dots, it is possible to place individual nanoparticles onto targeted locations, one nanoparticle per dot. Figure 24B shows an SEM image where ~20 nm Au nanoparticles were funneled into the center area of square-shaped guiding patterns, one Au nanoparticle per square-shaped pattern. The electrostatic funneling method is not constrained to rely on surface patterns but is also effective for three-dimensional structures having appropriate guiding geometry. An example is shown in Fig. 24C, where ~50 nm Au nanoparticles were placed along the centers of the exposed silicon oxide stripe made in a three-dimensional step structure.

Molecular Gradient Patterns

As previously discussed, self-assembled monolayers (SAMs) can be used as templates where nanoscale building blocks can be selectively attracted. The interaction between the SAMs and the building blocks can be readily controlled by appropriate selection of the SAMs molecules. For example, either repulsive or attractive interaction can occur depending on the polarity of the tail group of the SAMs molecules. Furthermore, the interaction intensity can be tuned by appropriate mixing of polar and non-polar molecules. Controlling the gradient of interaction intensity, Hong and co-workers recently reported the focused placement of nanowires and carbon nanotubes into the center area of the SAMs pattern, leading to placement with much higher precision than the precision that the SAMs templates are defined [207]. They named this scheme the "lens effect" because the building blocks are directed or focused onto the small center regions of the patterns much as light is focused onto a small spot by optical lenses. This focusing effect was achieved by creating a gradient in the molecular density in the SAMs pattern using two kinds of molecules, one is cysteamine (amine terminated; positively charged) and the other 1-octadecanethiol (ODT; methyl terminated, non-polar). The concentration of cysteamine was maximum in the center of the SAMs pattern and decreased away from the center. This molecular gradient was achieved by stamping the cysteamine on a gold substrate and letting it diffuse across the surface, followed by backfilling with ODT molecules. Figure 25, where two types of samples are compared, one without molecular gradient and the other with molecular gradient, shows the effectiveness of their approach. For the uniform SAMs patterns, when the substrate was immersed in a solution of V_2O_5 nanowires, the V_2O_5 nanowires (negatively charged) were adsorbed uniformly over the cysteamine patterns, Fig. 25A. However, for the patterns with molecular gradient, the V_2O_5 nanowires were directed onto the center of SAMs lines, resulting in placement precision of ~80 nm even though the line width of the SAMs pattern was ~2 μm. Similar results were obtained for the placement of single-walled carbon nanotubes (SWNTs), Fig. 25C and D.

Electrodynamic Focusing of Charged Aerosols

If microscale or nanoscale electrostatic lenses could be made near the substrate, it may be possible for charged nanoscale building blocks to be directed and placed on the focal spots on the substrate, resulting in high precision placement of nanoscale building blocks. This approach has been demonstrated for charged aerosols by Choi and co-workers [208] and independently by Barry and Jacobs [209]. In the approach by Choi and co-workers, a silicon substrate which was pre-patterned with PMMA (holes and lines in a PMMA film) was put inside a chamber into which

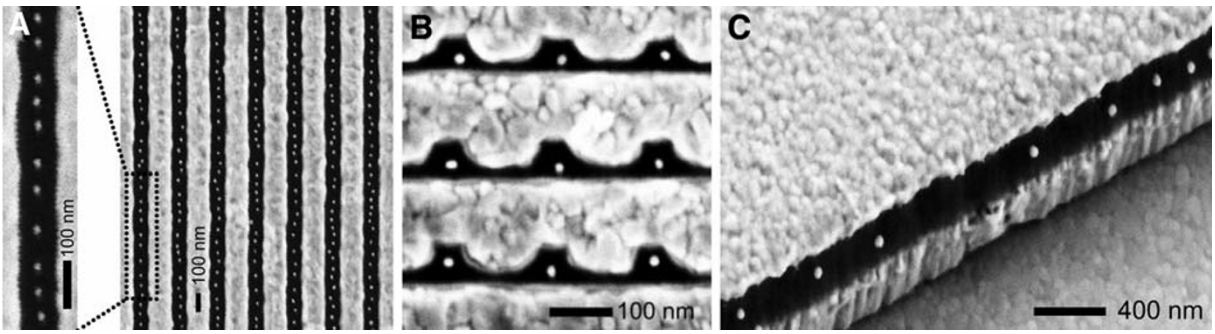

Fig. 24 Nanoparticle placement using electrostatic funneling scheme. (**A**) SEM image of Au nanoparticles (diameter ~20 nm) placed along the centers of silicon oxide lines using the electrostatic funneling scheme. (**B**) Zero-dimensional placement of individual nanoparticles (~20 nm diameter) onto the square-shaped pattern. Note that only one nanoparticle is placed in the center of each square-shaped pattern due to the repulsive electrostatic interactions between charged nanoparticles. (**C**) Nanoparticle placement in a step structure. Au nanoparticles (diameter ~50 nm) are placed along the center line of the exposed silicon oxide sidewall (dark stripe). For all SEM images: the patterns in dark, silicon oxide functionalized with APTES SAMs; the bright area, gold surface functionalized with MHA SAMs. The Au nanoparticles appear as bright dots. (Reprinted with permission from Reference [82]. Copyright 2007 American Chemical Society.)

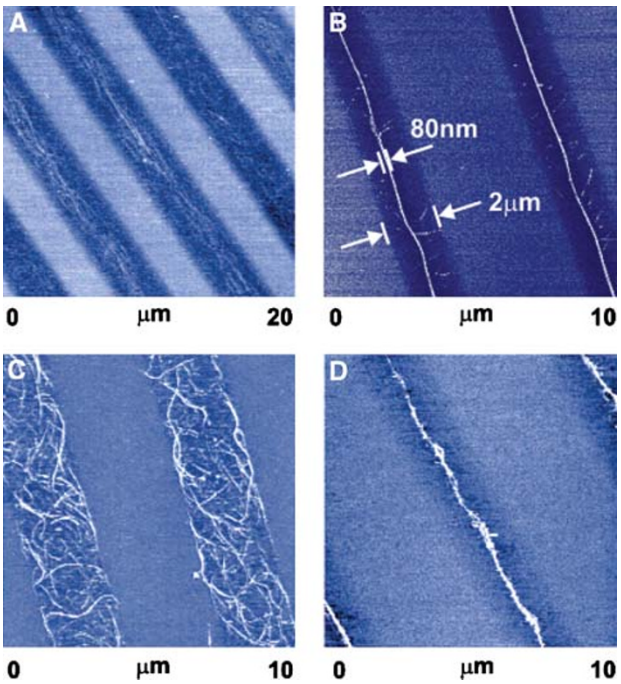

Fig. 25 AFM topography images of V_2O_5 nanowires and SWNTs on various SAM patterns. (**A**) V_2O_5 nanowires on uniform patterns comprised of ODT (bright area) and cysteamine (dark area). (**B**) V_2O_5 nanowires on the mixed SAM regions with gradient cysteamine surface molecular density on Au (ODT is utilized for passivation). (**C**) SWNTs on uniform cysteamine SAM patterns on Au. (**D**) SWNTs on gradient cysteamine patterns on Au. Theses patterns cover a large surface area ($\sim$1 cm $\times$ 1 cm) on the substrates. (Reprinted with permission from Reference [207]. Copyright 2006 American Chemical Society.)

an aerosol of positively charged silver nanoparticles and positively charged nitrogen ions was introduced with the substrate biased at –4 kV. During this process, the PMMA patterns were selectively charged with positive nitrogen ions because the nitrogen ions have two orders of magnitude higher mobility than the charged silver particles and they deposit much faster. The positively charged PMMA patterns worked as electrostatic lenses and guided the positively charged silver nanoparticles away from the PMMA patterns, leading to focused placement of nanoparticles. The nitrogen ions and silver particles arriving at the exposed silicon substrate were immediately neutralized since the silicon substrate was conductive. Figure 26 shows the effectiveness of this approach where they varied the nitrogen ion concentration introduced into the chamber, thereby changing the ion concentration on the PMMA patterns. Increased focusing effect is clearly seen as the nitrogen ion concentration introduced is increased. Note that although the dimension of the guiding structure (the diameter of the hole in the PMMA) is more than 200 nm, multiple numbers of 10 nm silver nanoparticles were directed and placed within a 35 nm circle, Fig. 26D. Using this approach, they demonstrated directed nanoparticle placement into the center locations of holes and lines in large-scale arrays of square (width: 230 nm) and line-shaped (line width: 230 nm) PMMA templates; using 10 nm silver particles, placement precision of $\sim$75 and $\sim$50 nm were demonstrated for arrays of squares and line patterns, respectively. Barry and Jacobs have also demonstrated the effectiveness of focused placement using PMMA and SiO_2 as electret materials [209]. The PMMA and SiO_2 were charged via built-in potential or through ion injection as verified by KFM (Kelvin probe force microscopy). They also exploited different types of nanoparticle sources, including evaporative, electrospray, and plasma, to create metallic and semiconducting nanoparticles of 10–50 nm in diameter and demonstrated focused nanoparticle placement with $\sim$50 nm lateral precision. For example, for $\sim$100 nm sized holes in corona-charged PMMA, 10–40 nm silver nanoparticles were placed onto center locations of the holes with a precision of $\sim$25 nm. For 300 nm wide trenches, gold nanoparticles were placed along the center locations of the trench lines with a precision of $\sim$75 nm.

Combination of Electrostatic Forces and Capillary Forces

Focused placement of spherical particles also can be achieved by exploiting both electrostatic forces and capillary forces. Using microscale polystyrene (PS) spheres as model systems, Aizenberg et al. have demonstrated a focused assembly of PS spheres ($\sim$1 μm in diameter) onto small targeted spots using a two-step process; first, electrostatic attachment of the particles onto functionalized surface patterns of circular shape, then rearrangement of the attached particles toward the center area of the circular patterns [210]. The functionalized surface patterns were made using μCP [78], which created patterns with negatively charged SAMs, and the remainder with positively charged SAMs. When the sample was immersed into the PS colloid in water, the PS particles (positively charged with amidine termination) selectively attached onto the negatively charged areas. In this process, the long-range electrostatic interaction (the electrical double-layer interaction [211, 212]) repelled the particles away from the positively charged SAMs and pushed them toward the center region of the pattern that was charged negatively, resulting in the first stage focusing effect. Second stage focusing effect, which is more dominant, was achieved during the drying process when the immersed sample was pulled from the colloid, rinsed, and allowed to dry. While the sample was drying, they monitored the movement of PS particles in real time using an optical microscope, which revealed dynamic rearrangement of particles toward to the center region of the circular patterns. This rearrangement,

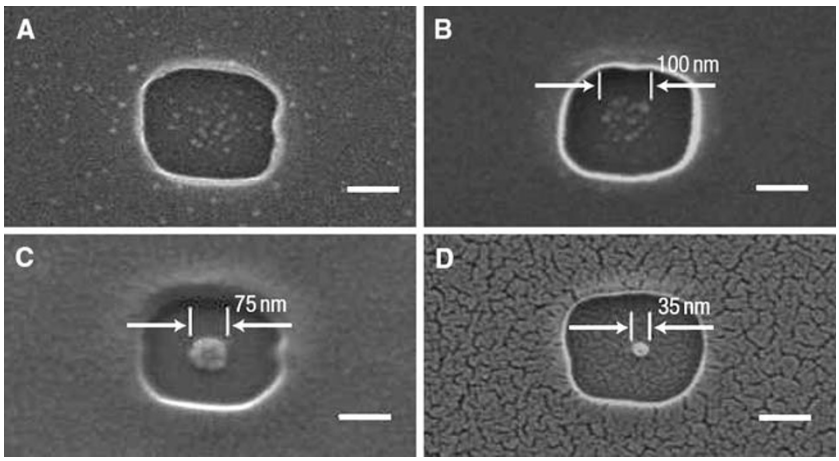

Fig. 26 Control of focusing with an increase of N_2 ion flow rate on a substrate with 230-nm-wide and 135-nm-thick PMMA patterns. Scale bars: 100 nm. (**A**) Particle deposition with no ion injection. (**B**–**D**) Particle deposition with ion injection: 3 L/min (ion concentration: $\sim 3.31 \times 10^5$ cm^{-3}), 4 L/min (ion concentration: $\sim 4.73 \times 10^5$ cm^{-3}), and 6 L/min (ion concentration: $\sim 6.13 \times 10^5$ cm^{-3}) for (**B**), (**C**), and (**D**), respectively. For all, an aerosol of 10 nm Ag nanoparticles was used. (Reprinted with permission from Reference [208]. Copyright 2006 Macmillan Publishers Ltd.)

the second focusing effect, was attributed to lateral capillary forces that were created when water–air interfaces formed asymmetrically on the particle surfaces during the drying process.

This combination of electrostatic and capillary forces was further utilized for controlled assembly of ordered two-dimensional patterns of *single* colloidal spheres. Figure 27 demonstrates a directed placement (focusing effect) of positively charged 1 μm spheres onto a square array of negatively charged circular patterns, where the circle diameter is 2.9 μm and the distance between the circle centers is 10 μm. The focusing effect is clearly seen in Fig. 27B, where the locations of the sphere centers were superimposed into one plot, with the outer circle representing the boundary of the negatively charged pattern (2.9 μm in diameter). Figure 27C is a schematic of the proposed mechanism of particle ordering in which the lateral capillary force pushes the particle toward the center of the circular pattern. When a particle is located off the center of the circular pattern, the deformation of water layer is asymmetric, resulting in asymmetric contact angle. This produces a net lateral force toward the center until the particle migrates into the center of the circular pattern. Placement precision of ~ 0.25 μm has been accomplished using charged circular patterns of diameter ~ 1.5 μm, a factor of 6 focusing efficiency.

Precision Placement Using Polymer Micelles

Polymer micelles containing nanoparticles in their cores can be used for high precision placement of nanoparticles when combined with template-assisted placement schemes described earlier. In an approach by Spatz et al. [213],

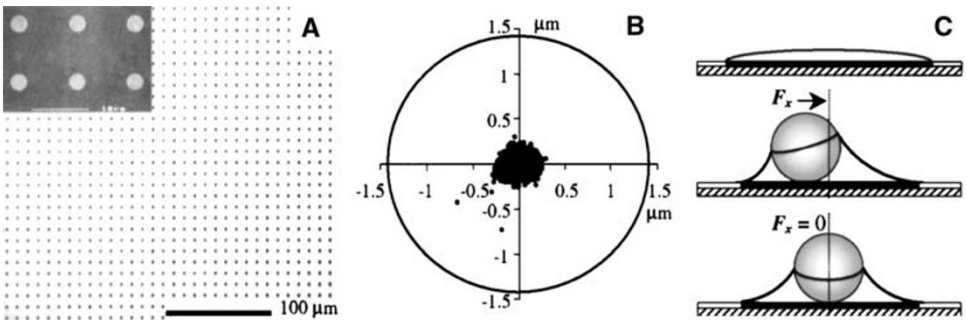

Fig. 27 Fabrication of ordered 2D arrays of single colloidal particles. (**A**) Light micrograph of a sample array; the inset shows a SEM of the template structure. (**B**) Mapped distribution of particles demonstrating a high degree of focusing within the outlined circle. (**C**) Schematic presentation of the proposed mechanism of particle ordering. (Reprinted with permission from Reference [210]. Copyright 2000 American Physical Society.)

physical templates such as holes and grooves were first patterned on a PMMA film using e-beam lithography. Polymer micelles, whose size were comparable to the hole diameter or trench width of the templates, were prepared [203] and spin-coated on the patterned PMMA film. During solvent evaporation, the micelles were pushed into holes and grooves by capillary forces. By systematically controlling the hole size, PMMA thickness, and concentration of micelles, they were able to place single micelles in each hole (diameter ~200 nm). Dissolution of the PMMA in acetone (lift-off) removed all micelles located on top of PMMA film that failed to go into holes and grooves. Exposure of the template to oxygen plasma removed the polymers selectively, leaving behind the nanoparticles which were loaded into the cores of the micelles. Using this approach, they were able to place individual nanoparticles on pre-defined locations of either periodic or aperiodic patterns. Figure 28 shows one example where single 7 nm Au nanoparticles were precisely placed on targeted substrate locations with a precision of better than 10 nm. It is worth noting that this nanoscale precision was obtained with much coarser template size; the diameter of the template holes made in the PMMA film was ~200 nm, comparable to the diameter of the starting polymer micelles.

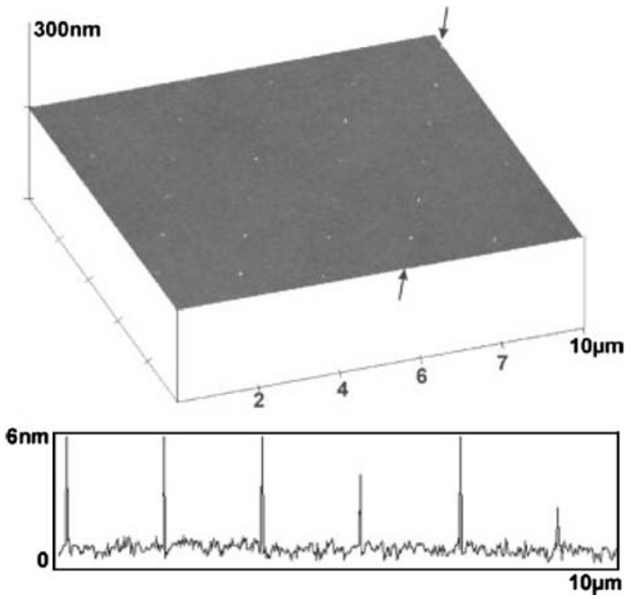

Fig. 28 Three-dimensional AFM image of single Au nanoparticles with a diameter of 7 nm separated by 2 μm. The two arrows in the image indicate the line along which the height profile was taken. The 10 μm line crosses six individual Au clusters, which corresponds to a positioning accuracy better than 10 nm. (Reprinted with permission from Reference [213]. Copyright 2002 Wiley-VCH.)

Summary

We have reviewed recent advances in various strategies for the controlled placement/growth of nanoscale building blocks. These were discussed in the context of seven categories; (1) placement using physical templates, (2) placement using molecular templates, (3) placement using electrostatic templates, (4) DNA-programmed placement, (5) placement using dielectrophoresis, (6) self-assembly of non-close-packed structure, and (7) focused placement. For the placement scheme using physical templates, we reviewed various approaches utilizing capillary forces, spin-coating, step-edges of crystalline metal and semiconductor surfaces, and sonication-assisted solution embossing. These methods allow controlled placement of spherical particles in the range of a few nanometers to several micrometers, nanometer scale non-spherical shape building blocks, nanofibers, and metal/metal-oxide nanowires. We also reviewed the formation/growth of 2D QD arrays utilizing underlying pre-defined patterns. A near-perfect yield of QD arrays has been demonstrated over a large area with a narrow size distribution.

Molecular templates (patterned SAMs) allow controlled placement of various nanoentities including nanoscale and microscale particles, carbon nanotubes, nanowires, proteins, viruses, and DNA. Patterning SAMs can be realized via selective attachment, removal, and/or modification of SAMs molecules. The associated techniques for SAMs patterning include microcontact printing (μCP), dip-pen nanolithography (DPN), scanning tunneling microscopy (STM), atomic force microscopy (AFM), and irradiation with deep UV light or electron-beams. Placement precision of up to a few tens of nanometers was achieved using these approaches.

Placement using electrostatic templates utilizes electret materials to create charge patterns onto which charged building blocks are selectively attracted. The charging methods include electrical microcontact printing (e-μCP), electron-beam writing, ion-beam writing, and writing using a conductive AFM tip. Placement precision of a few tens of nanometers has been demonstrated using these approaches.

The molecular recognition capability of DNA has been utilized to form one- or two-dimensional arrays of nanoscale building blocks. Single-stranded DNA has been used to form one-dimensional arrays of nanoparticles, proteins, and organometallic compounds. Rigid artificial DNA motifs (DNA tiles) have been synthesized via reciprocal exchanges. The DNA tiles have been built into 2D DNA crystals through programmed matching of sticky ends in DNA tiles. Utilizing DNA crystals as scaffolds, 2D arrays of nanoparticles, proteins, and peptide–antibodies have been constructed.

Dielectrophoresis has been exploited to manipulate uncharged nanoscale objects in dielectric liquid medium. The control of dielectrophoresis with many parameters, such as dielectric constants of an object and its surrounding medium, magnitude and frequency of applied electric field, and electric field gradient, has been discussed. Special attention has been paid to utilizing dielectrophoresis to place one-dimensional objects (such as nanowires and carbon nanotubes) between two electrodes, which is essential for fabrication of nanoelectronic devices and sensors. A recent advance has demonstrated self-limiting deposition of single SWNTs across electrode pairs with more than 90% yield over a large area.

Self-assembly of spherical particles to non-close-packed (ncp) structure provides an important pathway to large-scale placement of nanoscale or microscale particles with a variety of spatial configuration and varying lattice parameters. Two advances were discussed in this article; one is based on geometrical change of PDMS films either by expansion in solvent or mechanical stretching. The other uses polymer micelles whose core either contains or reduces to metal or metal-oxide nanoparticles. Control of nanoparticle diameter and lattice spacing of nanoparticle arrays was demonstrated by appropriate selection of block copolymers.

Focused placement approaches allow placement of nanoscale building blocks with precision much higher than the precision with which guiding templates are defined. This approach includes electrostatic funneling, placement using molecular gradient patterns, electrodynamic focusing of charged aerosols, guided placement using the synergy of electrostatic force and capillary force, and precision placement using polymer micelles. The important merit of these focused placement approaches is that large scale placement with nanoscale precision can be accomplished because the guiding structures can be defined on the scale of a few hundreds nanometers using conventional lithography. Placement precision of less than 10 nm was demonstrated over large areas using guiding structures on the scale of $\sim$100 nm.

Although the materials covered in this review are only a small portion of vast research effort on-going or performed over the last decade or so, it is quite clear that there are already many techniques that are maturing and have potential for practical implementation. Considering the accelerating speed of new discoveries and developments in this field, we may anticipate practical devices or sensors based on nanoscale building blocks being a reality in the near future.

Acknowledgements The author gratefully acknowledges Dr. Nancy Michael for valuable discussions. This work was supported in part by the Office of Naval Research (N00014-05-1-0030), National Science Foundation CAREER Grant (ECS-0449958), and Advanced Research Program of Texas Higher Education Coordinating Board (003656-0014-2006).

References

1. A. Javey, J. Guo, Q. Wang, M. Lundstrom, H.J. Dai, Nature **424**, 654 (2003)
2. A. Bachtold, P. Hadley, T. Nakanishi, C. Dekker, Science **294**, 1317 (2001)
3. D.L. Klein, R. Roth, A.K.L. Lim, A.P. Alivisatos, P.L. McEuen, Nature **389**, 699 (1997)
4. S.J. Wind, J. Appenzeller, R. Martel, V. Derycke, P. Avouris, Appl. Phys. Lett. **80**, 3817 (2002)
5. N.R. Franklin, Q. Wang, T.W. Tombler, A. Javey, M. Shim, H. Dai, Appl. Phys. Lett. **81**, 913 (2002)
6. X. Duan, Y. Huang, Y. Cui, J. Wang, C.M. Lieber, Nature **409**, 66 (2001)
7. A. Javey, Q. Wang, A. Ural, Y. Li, H. Dai, Nano Lett. **2**, 929 (2002)
8. Y. Huang, X. Duan, Y. Cui, L.J. Lauhon, K.-H. Kim, C.M. Lieber, Science **294**, 1313 (2001)
9. J. Wang, M.S. Gudiksen, X. Duan, Y. Cui, C.M. Lieber, Science **293**, 1455 (2001)
10. Y. Cui, Q. Wei, H. Park, C.M. Lieber, Science **293**, 1289 (2001)
11. J.A. Misewich, R. Martel, P. Avouris, J.C. Tsang, S. Heinze, J. Tersoff, Science **300**, 783 (2003)
12. A. Javey, H. Kim, M. Brink, Q. Wang, A. Ural, J. Guo, P. Mcintyre, P. McEuen, M. Lundstrom, H. Dai, Nat. Mater. **1**, 241 (2002)
13. X. Duan, Y. Huang, C.M. Lieber, Nano Lett. **2**, 487 (2002)
14. N.I. Kovtyukhova, B.K. Kelley, T.E. Mallouk, J. Am. Chem. Soc. **126**, 12738 (2004)
15. For a brief overview, see S.J. Koh, JOM **59**, 22 (2007)
16. Y.N. Xia, Y.D. Yin, Y. Lu, J. McLellan, Adv. Funct. Mater. **13**, 907 (2003)
17. Y. Cui, M.T. Bjork, J.A. Liddle, C. Sonnichsen, B. Boussert, A.P. Alivisatos, Nano Lett. **4**, 1093 (2004)
18. M.J. Gordon, D. Peyrade, Appl. Phys. Lett. **89**, 053112 (2006)
19. Y.D. Yin, Y.N. Xia, J. Am. Chem. Soc. **125**, 2048 (2003)
20. Y. Lu, Y.D. Yin, Y.N. Xia, Adv. Mater. **13**, 34 (2001)
21. Y.D. Yin, Y. Lu, Y.N. Xia, J. Am. Chem. Soc. **123**, 771 (2001)
22. G. Costantini, A. Rastelli, C. Manzano, P. Acosta-Diaz, R. Songmuang, G. Katsaros, O. Schmidt, K. Kern, Phys. Rev. Lett. **96**, 226106 (2006)
23. M.A. Kastner, Phys. Today **46**, 24 (1993)
24. A.P. Alivisatos, Science **271**, 933 (1996)
25. A.O. Orlov, I. Amlani, G.H. Bernstein, C.S. Lent, G.L. Snider, Science **277**, 928 (1997)
26. A. Zrenner, E. Beham, S. Stufler, F. Findeis, M. Bichler, G. Abstreiter, Nature **418**, 612 (2002)
27. C. Emary, L.J. Sham, Phys. Rev. B **75**, 125317 (2007)
28. P. Michler, A. Kiraz, C. Becher, W.V. Schoenfeld, P.M. Petroff, L.D. Zhang, E. Hu, A. Imamoglu, Science **290**, 2282 (2000)
29. Z.L. Yuan, B.E. Kardynal, R.M. Stevenson, A.J. Shields, C.J. Lobo, K. Cooper, N.S. Beattie, D.A. Ritchie, M. Pepper, Science **295**, 102 (2002)
30. S. Kiravittaya, M. Benyoucef, R. Zapf-Gottwick, A. Rastelli, O.G. Schmidt, Appl. Phys. Lett. **89**, 233102 (2006)
31. H. Sunamura, N. Usami, Y. Shiraki, S. Fukatsu, Appl. Phys. Lett. **66**, 3024 (1995)
32. P. Schittenhelm, M. Gail, J. Brunner, J.F. Nutzel, G. Abstreiter, Appl. Phys. Lett. **67**, 1292 (1995)
33. M. Henini, Nanoscale Res. Lett. **1**, 32 (2006)

34. S. Kiravittaya, R. Songmuang, A. Rastelli, H. Heidemeyer, O.G. Schmidt, Nanoscale Res. Lett. **1**, 1 (2006)
35. J. Stangl, V. Holy, G. Bauer, Rev. Mod. Phys. **76**, 725 (2004)
36. S. Kiravittaya, H. Heidemeyer, O.G. Schmidt, Appl. Phys. Lett. **86**, 263113 (2005)
37. S. Kiravittaya, O.G. Schmidt, Appl. Phys. Lett. **86**, 206101 (2005)
38. Z.Y. Zhong, G. Bauer, Appl. Phys. Lett. **84**, 1922 (2004)
39. Z.Y. Zhong, A. Halilovic, M. Muhlberger, F. Schaffler, G. Bauer, Appl. Phys. Lett. **82**, 445 (2003)
40. Z.Y. Zhong, A. Halilovic, T. Fromherz, F. Schaffler, G. Bauer, Appl. Phys. Lett. **82**, 4779 (2003)
41. H. Heidemeyer, U. Denker, C. Muller, O.G. Schmidt, Phys. Rev. Lett. **91**, 196103 (2003)
42. T. Kitajima, B. Liu, S.R. Leone, Appl. Phys. Lett. **80**, 497 (2002)
43. G. Jin, J.L. Liu, K.L. Wang, Appl. Phys. Lett. **76**, 3591 (2000)
44. E.S. Kim, N. Usami, Y. Shiraki, Appl. Phys. Lett. **72**, 1617 (1998)
45. O.G. Schmidt, N.Y. Jin-Phillipp, C. Lange, U. Denker, K. Eberl, R. Schreiner, H. Grabeldinger, H. Schweizer, Appl. Phys. Lett. **77**, 4139 (2000)
46. S. Kiravittaya, H. Heidemeyer, O.G. Schmidt, Physica E **23**, 253 (2004)
47. H. Heidemeyer, C. Muller, O.G. Schmidt, J. Cryst. Growth **261**, 444 (2004)
48. Q.H. Xie, A. Madhukar, P. Chen, N.P. Kobayashi, Phys. Rev. Lett. **75**, 2542 (1995)
49. J. Tersoff, C. Teichert, M.G. Lagally, Phys. Rev. Lett. **76**, 1675 (1996)
50. Z.Y. Zhong, A. Halilovic, M. Muhlberger, F. Schaffler, G. Bauer, J. Appl. Phys. **93**, 6258 (2003)
51. H. Heidemeyer, C. Muller, O.G. Schmidt, Physica E **23**, 237 (2004)
52. D.Y. Xia, A. Biswas, D. Li, S.R.J. Brueck, Adv. Mater. **16**, 1427 (2004)
53. H. Roder, E. Hahn, H. Brune, J.P. Bucher, K. Kern, Nature **366**, 141 (1993)
54. P. Gambardella, M. Blanc, H. Brune, K. Kuhnke, K. Kern, Phys. Rev. B **61**, 2254 (2000)
55. T. Jung, R. Schlittler, J.K. Gimzewski, F.J. Himpsel, Appl. Phys. A **61**, 467 (1995)
56. D.Y. Petrovykh, F.J. Himpsel, T. Jung, Surf. Sci. **407**, 189 (1998)
57. T. Jung, Y.W. Mo, F.J. Himpsel, Phys. Rev. Lett. **74**, 1641 (1995)
58. Y.W. Mo, F.J. Himpsel, Phys. Rev. B **50**, 7868 (1994)
59. M.P. Zach, K.H. Ng, R.M. Penner, Science **290**, 2120 (2000)
60. F. Favier, E.C. Walter, M.P. Zach, T. Benter, R.M. Penner, Science **293**, 2227 (2001)
61. R.M. Penner, J. Phys. Chem. B **106**, 3339 (2002)
62. A.M. Hung, S.I. Stupp, Nano Lett. **7**, 1165 (2007)
63. J.C. Love, L.A. Estroff, J.K. Kriebel, R.G. Nuzzo, G.M. Whitesides, Chem. Rev. **105**, 1103 (2005)
64. A. Ulman, Chem. Rev. **96**, 1533 (1996)
65. S. Onclin, B.J. Ravoo, D.N. Reinhoudt, Angew. Chem. Int. Ed. **44**, 6282 (2005)
66. F. Schreiber, J. Phys.-Condens. Mater. **16**, R881 (2004)
67. D.L. Allara, R.G. Nuzzo, Langmuir **1**, 45 (1985)
68. D.L. Allara, R.G. Nuzzo, Langmuir **1**, 52 (1985)
69. R.K. Smith, P.A. Lewis, P.S. Weiss, Prog. Surf. Sci. **75**, 1 (2004)
70. X.M. Li, J. Huskens, D.N. Reinhoudt, J. Mater. Chem. **14**, 2954 (2004)
71. Y.F. Gao, K. Koumoto, Crystal Growth Design **5**, 1983 (2005)
72. J.J. Gooding, F. Mearns, W.R. Yang, J.Q. Liu, Electroanalysis **15**, 81 (2003)
73. S. Kramer, R.R. Fuierer, C.B. Gorman, Chem. Rev. **103**, 4367 (2003)
74. D.S. Ginger, H. Zhang, C.A. Mirkin, Angew. Chem. Int. Ed. **43**, 30 (2004)
75. R.M. Nyffenegger, R.M. Penner, Chem. Rev. **97**, 1195 (1997)
76. B.D. Gates, Q.B. Xu, M. Stewart, D. Ryan, C.G. Willson, G.M. Whitesides, Chem. Rev. **105**, 1171 (2005)
77. R. Garcia, R.V. Martinez, J. Martinez, Chem. Soc. Rev. **35**, 29 (2006)
78. A. Kumar, G.M. Whitesides, Appl. Phys. Lett. **63**, 2002 (1993)
79. A. Kumar, H.A. Biebuyck, G.M. Whitesides, Langmuir **10**, 1498 (1994)
80. R.D. Piner, J. Zhu, F. Xu, S.H. Hong, C.A. Mirkin, Science **283**, 661 (1999)
81. P.E. Laibinis, J.J. Hickman, M.S. Wrighton, G.M. Whitesides, Science **245**, 845 (1989)
82. L.C. Ma, R. Subramanian, H.W. Huang, V. Ray, C.U. Kim, S.J. Koh, Nano Lett. **7**, 439 (2007)
83. M.S. Chen, C.S. Dulcey, L.A. Chrisey, W.J. Dressick, Adv. Funct. Mater. **16**, 774 (2006)
84. M.C. Howland, A.R. Sapuri-Butti, S.S. Dixit, A.M. Dattelbaum, A.P. Shreve, A.N. Parikh, J. Am. Chem. Soc. **127**, 6752 (2005)
85. Y.T. Kim, A.J. Bard, Langmuir **8**, 1096 (1992)
86. C.B. Ross, L. Sun, R.M. Crooks, Langmuir **9**, 632 (1993)
87. R.V. Martinez, F. Garcia, R. Garcia, E. Coronado, A. Forment-Aliaga, F.M. Romero, S. Tatay, Adv. Mater. **19**, 291 (2007)
88. S. Hoeppener, J.H.K. van Schaik, U.S. Schubert, Adv. Funct. Mater. **16**, 76 (2006)
89. J.C. Garno, Y.Y. Yang, N.A. Amro, S. Cruchon-Dupeyrat, S.W. Chen, G.Y. Liu, Nano Lett. **3**, 389 (2003)
90. R. Maoz, E. Frydman, S.R. Cohen, J. Sagiv, Adv. Mater. **12**, 725 (2000)
91. S.T. Liu, R. Maoz, J. Sagiv, Nano Lett. **4**, 845 (2004)
92. Z.M. Fresco, J.M.J. Frechet, J. Am. Chem. Soc. **127**, 8302 (2005)
93. C.S. Dulcey, J.H. Georger, V. Krauthamer, D.A. Stenger, T.L. Fare, J.M. Calvert, Science **252**, 551 (1991)
94. S. Hoeppener, R. Maoz, S.R. Cohen, L.F. Chi, H. Fuchs, J. Sagiv, Adv. Mater. **14**, 1036 (2002)
95. S.T. Liu, R. Maoz, G. Schmid, J. Sagiv, Nano Lett. **2**, 1055 (2002)
96. S.G. Rao, L. Huang, W. Setyawan, S.H. Hong, Nature **425**, 36 (2003)
97. J.B. Hannon, A. Afzali, C. Klinke, P. Avouris, Langmuir **21**, 8569 (2005)
98. J. Tien, A. Terfort, G.M. Whitesides, Langmuir **13**, 5349 (1997)
99. C.L. Feng, G.J. Vancso, H. Schonherr, Adv. Funct. Mater. **16**, 1306 (2006)
100. J.M. Zhang, Y.F. Ma, S. Stachura, H.X. He, Langmuir **21**, 4180 (2005)
101. J. Lahiri, E. Ostuni, G.M. Whitesides, Langmuir **15**, 2055 (1999)
102. P.C. Hidber, W. Helbig, E. Kim, G.M. Whitesides, Langmuir **12**, 1375 (1996)
103. L.M. Demers, D.S. Ginger, S.J. Park, Z. Li, S.W. Chung, C.A. Mirkin, Science **296**, 1836 (2002)
104. X.G. Liu, L. Fu, S.H. Hong, V.P. Dravid, C.A. Mirkin, Adv. Mater. **14**, 231 (2002)
105. L.M. Demers, C.A. Mirkin, Angew. Chem. Int. Ed. **40**, 3069 (2001)
106. S.W. Lee, B.K. Oh, R.G. Sanedrin, K. Salaita, T. Fujigaya, C.A. Mirkin, Adv. Mater. **18**, 1133 (2006)
107. R.A. Vega, D. Maspoch, K. Salaita, C.A. Mirkin, Angew. Chem. Int. Ed. **44**, 6013 (2005)
108. S.L. Zou, D. Maspoch, Y.H. Wang, C.A. Mirkin, G.C. Schatz, Nano Lett. **7**, 276 (2007)

109. Y.H. Wang, D. Maspoch, S.L. Zou, G.C. Schatz, R.E. Smalley, C.A. Mirkin, Proc. Natl. Acad. Sci. USA **103**, 2026 (2006)
110. R. Garcia, M. Tello, Nano Lett. **4**, 1115 (2004)
111. U. Schmelmer, A. Paul, A. Kuller, M. Steenackers, A. Ulman, M. Grunze, A. Golzhauser, R. Jordan, Small **3**, 459 (2007)
112. A. Turchanin, M. El-Desawy, A. Golzhauser, Appl. Phys. Lett. **90**, 053102 (2007)
113. T. Ye, E.A. McArthur, E. Borguet, J. Phys. Chem. B **109**, 9927 (2005)
114. T. Nakanishi, Y. Masuda, K. Koumoto, Chem. Mater. **16**, 3484 (2004)
115. K. Salaita, Y.H. Wang, J. Fragala, R.A. Vega, C. Liu, C.A. Mirkin, Angew. Chem. Int. Ed. **45**, 7220 (2006)
116. D. Bullen, S.W. Chung, X.F. Wang, J. Zou, C.A. Mirkin, C. Liu, Appl. Phys. Lett. **84**, 789 (2004)
117. K. Salaita, S.W. Lee, X.F. Wang, L. Huang, T.M. Dellinger, C. Liu, C.A. Mirkin, Small **1**, 940 (2005)
118. S. Lenhert, P. Sun, Y.H. Wang, H. Fuchs, C.A. Mirkin, Small **3**, 71 (2007)
119. P. Vettiger, M. Despont, U. Drechsler, U. Durig, W. Haberle, M.I. Lutwyche, H.E. Rothuizen, R. Stutz, R. Widmer, G.K. Binnig, IBM J. Res. Dev. **44**, 323 (2000)
120. P. Vettiger, G. Cross, M. Despont, U. Drechsler, U. Durig, B. Gotsmann, W. Haberle, M.A. Lantz, H.E. Rothuizen, R. Stutz, G.K. Binnig, IEEE Trans. Nanotechnol. **1**, 39 (2002)
121. E. Eleftheriou, T. Antonakopoulos, G.K. Binnig, G. Cherubini, M. Despont, A. Dholakia, U. Durig, M.A. Lantz, H. Pozidis, H.E. Rothuizen, P. Vettiger, IEEE Trans. Magn. **39**, 938 (2003)
122. H.O. Jacobs, G.M. Whitesides, Science **291**, 1763 (2001)
123. H.J. Mamin, B.D. Terris, L.S. Fan, S. Hoen, R.C. Barrett, D. Rugar, IBM J. Res. Dev. **39**, 681 (1995)
124. W.M.D. Wright, D.G. Chetwynd, Nanotechnology **9**, 133 (1998)
125. R.C. Barrett, C.F. Quate, J. Appl. Phys. **70**, 2725 (1991)
126. S. Iwamura, Y. Nishida, K. Hashimoto, IEEE Trans. Electron Devices **28**, 854 (1981)
127. M.N. Wybourne, M.D. Yan, J.F.W. Keana, J.C. Wu, Nanotechnology **7**, 302 (1996)
128. B.D. Terris, R.C. Barrett, IEEE Trans. Electron Devices **42**, 944 (1995)
129. C.R. Barry, J. Gu, H.O. Jacobs, Nano Lett. **5**, 2078 (2005)
130. T.B. Cao, Q.B. Xu, A. Winkleman, G.M. Whitesides, Small **1**, 1191 (2005)
131. Y.L. Loo, R.L. Willett, K.W. Baldwin, J.A. Rogers, J. Am. Chem. Soc. **124**, 7654 (2002)
132. M. Nonnenmacher, M.P. Oboyle, H.K. Wickramasinghe, Appl. Phys. Lett. **58**, 2921 (1991)
133. J. Joo, S. Moon, J.M. Jacobson, J. Vac. Sci. Technol. B **24**, 3205 (2006)
134. P.Y. Chi, H.Y. Lin, C.H. Liu, C.D. Chen, Nanotechnology **17**, 4854 (2006)
135. G.F. Dionne, J. Appl. Phys. **46**, 3347 (1975)
136. R. Renoud, F. Mady, C. Attard, J. Bigarre, J.P. Ganachaud, Phys. Status Solidi A **201**, 2119 (2004)
137. H. Fudouzi, M. Kobayashi, N. Shinya, Adv. Mater. **14**, 1649 (2002)
138. P. Mesquida, A. Stemmer, Adv. Mater. **13**, 1395 (2001)
139. S.D. Tzeng, K.J. Lin, J.C. Hu, L.J. Chen, S. Gwo, Adv. Mater. **18**, 1147 (2006)
140. N.C. Seeman, P.S. Lukeman, Rep. Prog. Phys. **68**, 237 (2005)
141. K. Tanaka, M. Shionoya, Chem. Lett. **35**, 694 (2006)
142. N.C. Seeman, Nature **421**, 427 (2003)
143. U. Feldkamp, C.M. Niemeyer, Angew. Chem. Int. Ed. **45**, 1856 (2006)
144. F.C. Simmel, W.U. Dittmer, Small **1**, 284 (2005)
145. K.V. Gothelf, T.H. LaBean, Org. Biomol. Chem. **3**, 4023 (2005)
146. E. Katz, I. Willner, Angew. Chem. Int. Ed. **43**, 6042 (2004)
147. N.C. Seeman, Chem. Biol. **10**, 1151 (2003)
148. C.M. Niemeyer, Angew. Chem. Int. Ed. **40**, 4128 (2001)
149. N.L. Rosi, C.A. Mirkin, Chem. Rev. **105**, 1547 (2005)
150. T.H. LaBean, H.Y. Li, Nano Today **2**, 26 (2007)
151. C.M. Niemeyer, T. Sano, C.L. Smith, C.R. Cantor, Nucleic Acids Res. **22**, 5530 (1994)
152. C.M. Niemeyer, W. Burger, J. Peplies, Angew. Chem. Int. Ed. **37**, 2265 (1998)
153. C.M. Niemeyer, Trends Biotechnol. **20**, 395 (2002)
154. K. Matsuura, M. Hibino, Y. Yamada, K. Kobayashi, J. Am. Chem. Soc. **123**, 357 (2001)
155. S.M. Waybright, C.P. Singleton, K. Wachter, C.J. Murphy, U.H.F. Bunz, J. Am. Chem. Soc. **123**, 1828 (2001)
156. C.J. Loweth, W.B. Caldwell, X.G. Peng, A.P. Alivisatos, P.G. Schultz, Angew. Chem. Int. Ed. **38**, 1808 (1999)
157. A.P. Alivisatos, K.P. Johnsson, X.G. Peng, T.E. Wilson, C.J. Loweth, M.P. Bruchez, P.G. Schultz, Nature **382**, 609 (1996)
158. Z.X. Deng, Y. Tian, S.H. Lee, A.E. Ribbe, C.D. Mao, Angew. Chem. Int. Ed. **44**, 3582 (2005)
159. T.J. Fu, N.C. Seeman, Biochemistry-US **32**, 3211 (1993)
160. X.J. Li, X.P. Yang, J. Qi, N.C. Seeman, J. Am. Chem. Soc. **118**, 6131 (1996)
161. F.R. Liu, R.J. Sha, N.C. Seeman, J. Am. Chem. Soc. **121**, 917 (1999)
162. E. Winfree, F.R. Liu, L.A. Wenzler, N.C. Seeman, Nature **394**, 539 (1998)
163. N.C. Seeman, Nano Lett. **1**, 22 (2001)
164. T.H. LaBean, H. Yan, J. Kopatsch, F.R. Liu, E. Winfree, J.H. Reif, N.C. Seeman, J. Am. Chem. Soc. **122**, 1848 (2000)
165. H. Yan, S.H. Park, G. Finkelstein, J.H. Reif, T.H. LaBean, Science **301**, 1882 (2003)
166. C.D. Mao, W.Q. Sun, N.C. Seeman, J. Am. Chem. Soc. **121**, 5437 (1999)
167. S.H. Park, C. Pistol, S.J. Ahn, J.H. Reif, A.R. Lebeck, C. Dwyer, T.H. LaBean, Angew. Chem. Int. Ed. **45**, 735 (2006)
168. J.W. Zheng, P.E. Constantinou, C. Micheel, A.P. Alivisatos, R.A. Kiehl, N.C. Seeman, Nano Lett. **6**, 1502 (2006)
169. B.A.R. Williams, K. Lund, Y. Liu, H. Yan, J.C. Chaput, Angew. Chem. Int. Ed. **46**, 3051 (2007)
170. S.H. Park, P. Yin, Y. Liu, J.H. Reif, T.H. LaBean, H. Yan, Nano Lett. **5**, 729 (2005)
171. H.Y. Li, S.H. Park, J.H. Reif, T.H. LaBean, H. Yan, J. Am. Chem. Soc. **126**, 418 (2004)
172. J. Sharma, R. Chhabra, Y. Liu, Y.G. Ke, H. Yan, Angew. Chem. Int. Ed. **45**, 730 (2006)
173. J.D. Le, Y. Pinto, N.C. Seeman, K. Musier-Forsyth, T.A. Taton, R.A. Kiehl, Nano Lett. **4**, 2343 (2004)
174. S.J. Xiao, F.R. Liu, A.E. Rosen, J.F. Hainfeld, N.C. Seeman, K. Musier-Forsyth, R.A. Kiehl, J. Nanopart. Res. **4**, 313 (2002)
175. H.A. Pohl, *Dielectrophoresis* (Cambridge, Cambridge University Press, 1978)
176. R. Krupke, F. Hennrich, H. von Lohneysen, M.M. Kappes, Science **301**, 344 (2003)
177. R. Krupke, F. Hennrich, H.B. Weber, M.M. Kappes, H. von Lohneysen, Nano Lett. **3**, 1019 (2003)
178. L.A. Nagahara, I. Amlani, J. Lewenstein, R.K. Tsui, Appl. Phys. Lett. **80**, 3826 (2002)
179. J.Y. Chung, K.H. Lee, J.H. Lee, R.S. Ruoff, Langmuir **20**, 3011 (2004)
180. R. Krupke, F. Hennrich, H.B. Weber, D. Beckmann, O. Hampe, S. Malik, M.M. Kappes, H.V. Lohneysen, Appl. Phys. A **76**, 397 (2003)
181. R.J. Barsotti, M.D. Vahey, R. Wartena, Y.M. Chiang, J. Voldman, F. Stellacci, Small **3**, 488 (2007)
182. G.H. Markx, Y. Huang, X.F. Zhou, R. Pethig, Microbiology **140**, 585 (1994)

183. J. Suehiro, G.B. Zhou, M. Imamura, M. Hara, IEEE Trans. Ind. Appl. **39**, 1514 (2003)
184. H.B. Li, R. Bashir, Sensor Actuat B-Chem. **86**, 215 (2002)
185. P.R.C. Gascoyne, X.B. Wang, Y. Huang, F.F. Becker, IEEE Trans. Ind. Appl. **33**, 670 (1997)
186. G.H. Markx, R. Pethig, Biotechnol. Bioeng. **45**, 337 (1995)
187. R. Holzel, N. Calander, Z. Chiragwandi, M. Willander, F.F. Bier, Phys. Rev. Lett. **95**, 128102 (2005)
188. Y.L. Liu, J.H. Chung, W.K. Liu, R.S. Ruoff, J. Phys. Chem. B. **110**, 14098 (2006)
189. T.B. Jones, *Electromechanics of Particles* (Cambridge, Cambridge University Press, 1995)
190. J.J. Boote, S.D. Evans, Nanotechnology **16**, 1500 (2005)
191. H.W. Seo, C.S. Han, S.O. Hwang, J. Park, Nanotechnology **17**, 3388 (2006)
192. X.Q. Chen, T. Saito, H. Yamada, K. Matsushige, Appl. Phys. Lett. **78**, 3714 (2001)
193. R.H. Zhou, H.C. Chang, V. Protasenko, M. Kuno, A.K. Singh, D. Jena, H. Xing, J. Appl. Phys. **101**, 073704 (2007)
194. A. Vijayaraghavan, S. Blatt, D. Weissenberger, M. Oron-Carl, F. Hennrich, D. Gerthsen, H. Hahn, R. Krupke, Nano Lett. **7**, 1556 (2007)
195. L.X. Benedict, S.G. Louie, M.L. Cohen, Phys. Rev. B **52**, 8541 (1995)
196. M.J. O'Connell, S.M. Bachilo, C.B. Huffman, V.C. Moore, M.S. Strano, E.H. Haroz, K.L. Rialon, P.J. Boul, W.H. Noon, C. Kittrell, J. Ma, R.H. Hauge, R.B. Weisman, R.E. Smalley, Science **297**, 593 (2002)
197. R. Micheletto, H. Fukuda, M. Ohtsu, Langmuir **11**, 3333 (1995)
198. T. Ogi, L.B. Modesto-Lopez, F. Iskandar, K. Okuyama, Colloids Surf. A-Physicochem. Eng. Aspects **297**, 71 (2007)
199. H.W. Deckman, J.H. Dunsmuir, S. Garoff, J.A. McHenry, D.G. Peiffer, J. Vac. Sci. Technol. B **6**, 333 (1988)
200. J.C. Hulteen, R.P. Vanduyne, J. Vac. Sci. Technol. A **13**, 1553 (1995)
201. Z.P. Huang, D.L. Carnahan, J. Rybczynski, M. Giersig, M. Sennett, D.Z. Wang, J.G. Wen, K. Kempa, Z.F. Ren, Appl. Phys. Lett. **82**, 460 (2003)
202. O.J. Cayre, V.N. Paunov, J. Mater. Chem. **14**, 3300 (2004)
203. J.P. Spatz, S. Mossmer, C. Hartmann, M. Moller, T. Herzog, M. Krieger, H.G. Boyen, P. Ziemann, B. Kabius, Langmuir **16**, 407 (2000)
204. X. Yan, J.M. Yao, G. Lu, X. Li, J.H. Zhang, K. Han, B. Yang, J. Am. Chem. Soc. **127**, 7688 (2005)
205. Z. Sun, B. Yang, Nanoscale Res. Lett. **1**, 46 (2006)
206. Here, we are interested in relative placement of building blocks with respect to the template. The placement precision is defined as the average deviation of positions of building blocks from the target position. For example, if a 100 nm width trench is used as a guiding structure and nanoparticles are randomly distributed within the trench, the placement precision would be comparable to 50/2 nm. On the other hand, if nanoparticles are located along the center line of the trench with average deviation from the center line being 5 nm, the placement precision is defined as 5 nm
207. S. Myung, J. Im, L. Huang, S.G. Rao, T. Kim, D.J. Lee, S.H. Hong, J. Phys. Chem. B **110**, 10217 (2006)
208. H. Kim, J. Kim, H.J. Yang, J. Suh, T. Kim, B.W. Han, S. Kim, D.S. Kim, P.V. Pikhitsa, M. Choi, Nat. Nanotechnol. **1**, 117 (2006)
209. C.R. Barry, H.O. Jacobs, Nano Lett. **6**, 2790 (2006)
210. J. Aizenberg, P.V. Braun, P. Wiltzius, Phys. Rev. Lett. **84**, 2997 (2000)
211. J. Israelachvili, *Intermolecular and Surface Forces*, 2nd edn. (London, Academic Press, 1991)
212. E.J.W. Verwey, J.T.G. Overbeek, *Theory of the Stability of Lyophobic Colloids* (Amsterdam, Elsevier, 1948)
213. J.P. Spatz, V.Z.H. Chan, S. Mossmer, F.M. Kamm, A. Plettl, P. Ziemann, M. Moller, Adv. Mater. **14**, 1827 (2002)